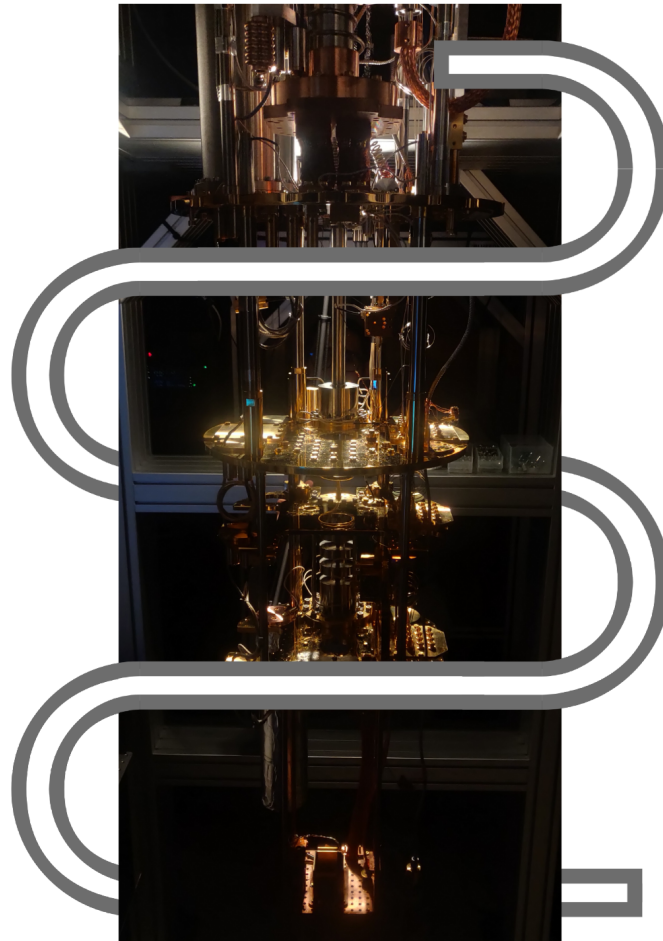




**CHALMERS**  
UNIVERSITY OF TECHNOLOGY



# **Towards flux-tunable superconducting coplanar waveguide resonators for inductive coupling to levitated superconducting particles**

AVAN MIRKHAN

---

DEPARTMENT OF MICROTECHNOLOGY AND NANOSCIENCE (MC2)

CHALMERS UNIVERSITY OF TECHNOLOGY

Gothenburg, Sweden 2022

[www.chalmers.se](http://www.chalmers.se)



THESIS FOR THE DEGREE OF MASTER OF SCIENCE 2022

**Towards flux-tunable superconducting coplanar waveguide  
resonators for inductive coupling to levitated  
superconducting particles**

AVAN MIRKHAN



**CHALMERS**  
UNIVERSITY OF TECHNOLOGY

Department of Microtechnology and Nanoscience (MC2)  
*Division of Quantum Technology Laboratories*  
CHALMERS UNIVERSITY OF TECHNOLOGY  
Gothenburg, Sweden 2022

Towards flux-tunable superconducting coplanar waveguide resonators for inductive coupling to levitated superconducting particles  
AVAN MIRKHAN

© AVAN MIRKHAN, 2022.

Supervisors: Achintya Paradkar & Martí Gutierrez Latorre, Department of Microtechnology and Nanoscience - MC2  
Examiner: Witlef Wieczorek, Department of Microtechnology and Nanoscience - MC2

Master's Thesis 2022  
Department of Microtechnology and Nanoscience - MC2  
Division of Quantum Technology Laboratories  
Wieczorek Group  
Chalmers University of Technology  
SE-412 96 Gothenburg  
Telephone +46 31 772 1000

Cover: Artistic depiction of a co-planar waveguide covering an image of the dilution refrigerator hosting the setup used for the experiments. Original picture taken and edited by author.

Typeset in L<sup>A</sup>T<sub>E</sub>X  
Printed by Chalmers Reproservice  
Gothenburg, Sweden 2022

Towards flux-tunable superconducting coplanar waveguide resonators for inductive coupling to levitated superconducting particle  
AVAN MIRKHAN  
Department of Microtechnology and Nanoscience - MC2  
Chalmers University of Technology

## Abstract

Superconducting magnetic levitation is a promising technique to study potential limits of quantum mechanics for mesoscopic objects due to the levitated object being extremely isolated from the environment. Using optomechanics techniques, the centre-of-mass motion of a levitated particle can be controlled and cooled down to its motional ground-state thereby bringing it into the quantum regime. This would enable macroscopic quantum experiments as well as ultra-sensitive force and acceleration sensing. In order to realize this, the motion of the particle's centre-of-mass would be coupled to a flux-tunable superconducting resonator, which would allow control of the particle motion through the state of the resonator. This thesis investigates the microwave properties of superconducting coplanar waveguide (CPW) resonators. At first, non-flux tunable CPW resonators were fabricated from Aluminum and Niobium and measured in a cryostat at mK temperatures. The best performing CPW resonators achieved unloaded quality factors of  $\sim 10^5$  and  $\sim 10^6$  at  $10^6$  average number of intra-cavity photons for Aluminum and Niobium, respectively. The quality factors of these resonators were found to be one order of magnitude lower for Al, but higher for Nb, when compared to the state-of-the-art. Subsequently, flux-tunable resonators were fabricated by embedding a SQUID into Aluminum-based CPW resonators. The flux tunability of these resonators was studied and was found to be much lower than expected. The reason for the low tunability was due to the fabrication process of the Josephson junctions of the embedded SQUID, in which the junction width was too wide causing an excess amount of aluminum to have deposited onto the substrate. Based on these identified issues, suggestions have been proposed to improve upon the fabrication of flux-tunable CPW resonators, such that in the future the desired frequency tuning through a change in magnetic flux can be observed.

Keywords: superconductivity, resonators, levitation, microwave engineering, magnetic flux, quality factors, quantum mechanics, flux modulation.



## Acknowledgements

”Rome was not built in one day” is a phrase that I have identify with quite a bit. Naturally, great things do take time to build and develop, but more importantly it takes more than a single person. The same goes for this thesis and the work that have been put into it. First and foremost, I am most humbled and in gratitude to my examiner, Associate Professor Witlef Wieczorek, who graciously accepted me to work in the 'maglev' team despite my limited experience. His inspiring enthusiasm and continuous support to the project taught me so much about the field of quantum physics. The most important lesson I have learned, is to have fun in the work that I am doing.

I am in awe of the patience of my supervisors Achintya Paradkar and Martí Gutierrez Latorre, and, in extension, Sushanth Kini from the optomechanics team. They have always found a way to answer my never-ending questions and helped me in the lab. In their own unique way of understanding the work and supervising me throughout the project, have I understood what it truly means being an experimental physicist. I would also like to thank everybody I have gotten to know in QTL, who did not hesitate to give their input to help my work, in particular: Chris, Christian, Janka, Amr, Anuj, Sandoko, Tom, Andreas, Robert, Daryoush, Anita, Giovanna, Lert, David, Claudia, Joey and Johan. You have all contributed with valuable knowledge, help and tools, but more importantly with an amazing work atmosphere.

I am immensely thankful to Göteborgs Förenade Studenkårer, in particular to Jack and Jonathan. Not only have they been understaning with me working on the thesis over the year, but they have been teaching me so much about what it means to actually being engaged and passionate in the work one is dealt with. In the same vein, I am grateful for my classmates in MPNAT21/22, in particular Ajša, Michael, Thanos, Paul, Awse, Saieesh, Núria, Victor and Fia, for sharing this experience with you all.

Lastly, I want to thank all my friends from home, at Chalmers, in Göteborg and all around the world. In particular, Felicia and Thim, you both have showed me nothing but love and support over my entire time at Chalmers, always kept me grounded and constantly pushed me to be the best version of myself. I am indebted to my parents, who have pushed me to achieve new heights, for their love and support over the years.

If I could wish for something regarding this thesis, it is for you, the reader, to learn or find something new or inspiring in the words that I have written. This is how the thesis fulfills its purpose.

Avan Mirkhan, Gothenburg, 2022



# Contents

<b>List of Figures</b>	<b>xi</b>
<b>1 Introduction</b>	<b>1</b>
1.1 Background . . . . .	1
1.2 Aim . . . . .	1
<b>2 Theory</b>	<b>3</b>
2.1 Superconductivity . . . . .	3
2.1.1 Josephson Junctions . . . . .	5
2.1.2 RF & DC SQUID . . . . .	5
2.2 Superconducting Resonators . . . . .	8
2.2.1 Co-planar waveguide resonators . . . . .	8
2.2.2 Transmission line impedance . . . . .	9
2.2.3 Quarter-wave resonators . . . . .	9
2.2.4 Scattering parameters . . . . .	11
2.2.5 Resonance Circles and model fit . . . . .	12
2.2.6 Derivation of intra-cavity Photon number . . . . .	14
2.3 Flux-tunable resonator . . . . .	15
2.4 Superconducting levitation . . . . .	16
2.4.1 Magnetic levitation of a superconducting particle . . . . .	17
2.4.2 Coupling of a levitating superconducting particle to a flux tunable resonator . . . . .	17
<b>3 Methodology</b>	<b>19</b>
3.1 Simulation of superconducting resonators . . . . .	19
3.2 Cryogenic measurements . . . . .	20
3.2.1 Cryostat . . . . .	20
3.2.2 Setup . . . . .	21
3.3 Device fabrication . . . . .	22
3.3.1 Fabrication of critical current density bridge and CPW . . . . .	22
3.3.1.1 Superconductor deposition . . . . .	22
3.3.1.2 Lithography and etching . . . . .	22
3.3.2 Fabrication of flux-tunable resonators . . . . .	23
3.3.2.1 Shadow evaporation . . . . .	23
3.3.2.2 Lithography and etching of contact pads . . . . .	23
3.4 Measurement Setup . . . . .	24
3.4.1 Determination of critical current density . . . . .	24
3.4.2 Resonator characterization . . . . .	24
3.4.2.1 Resonance frequency and quality factor . . . . .	24
3.4.2.2 Flux tunability . . . . .	25
<b>4 Results</b>	<b>27</b>
4.1 Superconducting properties of Al . . . . .	27
4.2 CPW Resonator characterization . . . . .	27
4.3 FTR characterization and flux tunability . . . . .	32
<b>5 Conclusions</b>	<b>35</b>
5.1 Summary . . . . .	35

5.2	Future work . . . . .	35
	<b>Bibliography</b>	<b>37</b>
	<b>A Appendix A</b>	<b>I</b>
A.1	Full derivation from $Z_{TLR}$ to $S_{21}(\omega_0)$ . . . . .	I
	<b>B Appendix B</b>	<b>V</b>
B.1	Current density and CPW resonator fabrication . . . . .	V
B.1.1	Aluminum . . . . .	V
B.1.2	Niobium . . . . .	V

# List of Figures

1.1	Schematic of the thesis aim, with a superconducting resonator circuit with an embedded SQUID, coupled to the levitating superconducting particle in a harmonic trap. . . . .	2
2.1	Illustration of the Meissner-Ochsenfeld effect of a superconducting sphere. <b>(a)</b> Magnetic flux threads through the sphere as $T > T_c$ . <b>(b)</b> When cooled below $T_c$ , magnetic flux is expelled from the superconductor. . . . .	3
2.2	Magnetization versus applied magnetic field of <b>(a)</b> a type-I and <b>(b)</b> a type-II superconductor. <b>(a)</b> For type-I superconductors, the material becomes normal conducting when the applied magnetic field is higher than $H_c$ . <b>(b)</b> For type-II superconductors, magnetic flux will penetrate the material if the applied magnetic field is higher than $H_{c1}$ . The superconductor is in a vortex state between $H_{c1}$ and $H_{c2}$ . The material is normal conducting above $H_{c2}$ . Dotted line is the response of an equivalent type-I material, shown for reference. . . . .	4
2.3	Schematics of a SIS junction. <b>(left)</b> The phase difference changes as wavefunction of the Cooper pairs tunnel through the junction. <b>(right)</b> The Cooper-pair density distribution around the junction. . . . .	5
2.4	Schematics of an (a) RF SQUID and (b) DC SQUID with an applied current. . .	5
2.5	$\Phi$ as a function of $\Phi_{\text{ext}}$ for <b>(a)</b> $\beta_L = 1$ and <b>(b)</b> $\beta_L > 1$ , where the hysteretical behavior appears. . . . .	6
2.6	$ I_M $ as a function of $\Phi_{\text{ext}}/\Phi_0$ . $I_M$ reaches peak values at integer values of $\Phi_{\text{ext}}/\Phi_0$	7
2.7	Cross-section of a co-planar waveguide. The central conductor, of width $W$ , is separated from the ground plane on either side by a width $S$ . The substrate is illustrated as yellow and the superconductor as gray. . . . .	8
2.8	<b>(left)</b> A meandered quarter-wave CPW resonator. One end is capacitively coupled to the feedline and the other end is shorted to ground. The central conductor for the resonator and transmission line have the same width and spacing between the central conductor and ground plane. <b>(right)</b> Schematic of the equivalent circuit of a resonator coupled to a feedline. . . . .	10
2.9	Network representation of the feedline in- (1) and out-port (2), as well as the resonator (3). The scattering is also depicted. . . . .	12
2.10	<b>(top)</b> Scattering magnitude and phase response for an ideal resonator, along with the resonance circle. The diameter of the circle is determined by the quality factor ratio $Q_I/ Q_C $ and the resonance frequency corresponds to the point where $\text{Im}(S_{21}) = 0$ (Model parameters: $\tau = 0$ ns, $\phi = 0, a = 1, \alpha = 0$ ). <b>(bottom)</b> The response data and circle are skewed due to environmental damping effects. Impedance mismatch results in an asymmetry of the resonance dip in the $ S_{21} $ curve, while the resonance circle distortion is caused by the electric delay from the cabling (Model parameters: $\tau = 100$ ns, $\phi = -0.5, a = 0.1, \alpha = 0.01$ ). . . . .	14
2.11	Schematic of a flux tunable resonator. $L_S$ is the SQUID-inductance given by $L_J$ and $L_g$ . . . . .	16
2.12	Frequency modulation as a function of externally applied flux for varying values of critical current of the JJ. For small $I_{c0}$ , $\omega_c$ never reaches $\omega_0$ due to $L_J$ being large. On the other hand, large $I_{c0}$ results in very sharp, but localized modulation of $\omega_c$ around $n\phi_0/2$ . . . . .	16

3.1	(a) Simulation of the ground plane. The bounding box is enclosing the resonator and a portion of the feedline. The mesh grid of inside the bounding box is much finer compared to the grid in the entire ground plane. (b) Normalized electric field distribution over one resonator. The electric field is normalized to $4 \times 10^{11}$ V/m. The voltage distribution is concentrated along the meandered resonator and is weakest at the ground-end. . . . .	19
3.2	A schematic representation of the dilution refrigerator and the experimental setup. The stages are: Room temperature (RT), 50 K, 4 K, Still ( $\sim 800$ mK), Cold plate (CP, $\sim 100$ mK) and Mixing chamber (MXC, $\sim 15$ mK). The CPW-devices are mounted inside a sample holder which is electrically shielding the devices, while a can around the sample holder provides the magnetic shielding. Port 1 sends signals to the device and port 2 receives signals returning to the VNA. . .	20
3.3	(a) The sample holder for the CPW and FTR devices. SMA connectors are attached to both sides of the box. (b) Magnetic shield can. The arrow points to where the sample holder lies within the can. . . . .	22
3.4	(a) Bridges of different widths. (b) A $\lambda/4$ CPW coupled to the feedline. . . . .	23
3.5	Schematic overview illustrating shadow evaporation. . . . .	23
3.6	A fabricated SQUID-cavity connected to the central conductor of the CPW. The junction electrodes are 400 nm in width and the loop size is $30 \times 30 \mu\text{m}^2$ . . . . .	24
3.7	Schematic of the experimental setup to determine $j_c$ . A DC source supplies current to the samples, which are near a RuOx-temperature sensor. . . . .	24
3.8	The scattering parameters of an ideal resonator described in Section 2.2.5 . . . . .	25
3.9	Schematic of the setup for measuring microwave transmission spectrum. The measured samples and microwave components are inside the dilution refrigerator. . . . .	25
3.10	Schematic of the setup for identifying the flux tunability. . . . .	26
4.1	Sample temperature as a function of applied current for a bridge with cross-section of $300 \times 0.3 \mu\text{m}^2$ . An abrupt increase in temperature is observed around 10 mA. . . . .	27
4.2	(a) Power sweep of an Al CPW resonator at $\omega_0 \approx 2\pi \times 5.15$ GHz from 20 dBm to -25 dBm VNA output power. $\omega_0$ shifts for varying powers. Superconductivity is broken at high powers. (b) Unsuccessful and successful model fits of measurement data for 20 and -15 dBm, respectively. . . . .	28
4.3	4 to 8 GHz measurement of the Al and Nb resonators. The black arrows mark the resonance frequencies of the CPW resonators. The arrow with a star is not a resonance frequency of any Al CPW resonators. . . . .	28
4.4	Analytic, simulated and measured resonance frequencies ( $\omega_0$ ), coupling ( $Q_c$ ) and measured internal ( $Q_i$ ) quality factors for CPW resonators of different lengths and materials, as a function of inverse resonator length. The experimental values correspond to $10^8$ and $10^6$ average number of intra-cavity photons for Al and Nb, respectively. The values obtained from simulations are independent of the superconducting material, as opposed to the analytic and experimental values. . . . .	29
4.5	Quality factors of Al and Nb resonators from 4 to 8 GHz as a function of intra-cavity photon number. (upper) The coupling quality factor is roughly constant for Nb, but decreases for lower powers for Al. (lower) The internal quality factor showing the losses. Both Al and Nb show similar trends. . . . .	31
4.6	(a) $Q_i$ as a function of circulating power and equivalent average number of intra-cavity photon numbers for superconducting Al CPW resonators on sapphire [38]. (b) $Q_i$ as a function of circulating power, with the equivalent average intra-cavity photon number, for superconducting Nb CPW resonators (hollow blue squares) deposited on top of a Si-substrate. [40]. . . . .	31
4.7	Analytic determination of the frequency modulation of the FTR for an external flux in the interval of $[-\Phi_0, \Phi_0]$ . The frequency modulation, $\partial\omega_0/\partial\Phi$ is marked as the dotted red tangent line at $0.8 \times \Phi_0$ . . . . .	32
4.8	$S_{21}$ transmission data of the FTR device made out of Al, as a function of frequency, measured at -106 dBm total power. Five resonance frequencies were detected, indicated by the arrows, out of which one is flux tunable, marked with the arrow with a diamond. The response at 7.4 GHz is the feedline frequency. . . . .	32

---

4.9	$S_{21}$ transmission as a function of frequency and biasing current. The resonance frequency is tuned at approximately $\omega_0 = 6.29 \times 2\pi$ GHz. . . . .	33
4.10	Frequency modulation of $\omega_0 = 2\pi \times 6.29$ GHz over one $\Phi_0$ , at varying power. The respective biasing current applied is also shown. The inset shows the corresponding portion of the $S_{21}$ transmission data in Figure 4.9. . . . .	33
4.11	(a) SEM image of the SQUID-loop. (b) SEM image of the JJs. The deposited edges of the junctions are connected. . . . .	34
5.1	A proposed experimental setup for the direct coupling experiment. The levitating superconducting particle is trapped inside a quadrupole magnetic field. The field that is modulated by the particle motion is directly fed to the FTR. . . . .	36



# 1

## Introduction

### 1.1 Background

The theory of quantum mechanics describes extremely precisely the most fundamental particles that are encountered in our world. Quantum superposition, entanglement and quantum tunneling, as foreign as they are to the understanding of the classical world, are some of the predictions that enabled technologies such as quantum computing and quantum sensing. However, there still are fundamental questions that need to be answered in the context of quantum mechanics, one of them being: Does a boundary between quantum mechanics and classical mechanics exist, and if so, where is it and what causes this boundary to appear?

There have been multiple approaches [1] to realize macroscopic quantum states, such as matter wave interferometry [2] and large spatial superposition states [3]. Recent works [4] suggest that a micrometer-sized particle could be used to generate large, and massive quantum spatial superpositions. To achieve this, the center-of-mass motion of the particle has to be in the ground state energy level. Assuming that the particle motion is thermally driven, the average number of phonons in the motion of the particle can be estimated from the following equation

$$\langle n_{\text{phonon}} \rangle = \frac{k_B T}{\hbar \omega}, \quad (1.1)$$

where  $k_B$  and  $T$  are the Boltzmann constant and the temperature, respectively,  $\hbar$  is the reduced Planck constant and  $\omega$  is the frequency of the particle's center-of-mass motion. To reach the ground state, that is  $\langle n_{\text{phonon}} \rangle < 1$ , given a frequency in the range of kHz, the ground state of the center-of-mass motion of the particle would have an equivalent temperature on the order of nK. Conventional cooling techniques, such as dilution refrigeration, reach down to mK temperatures at lowest, which is not enough to cool such a system to the ground state. Thus, other means are required to further cool down the center-of-mass motion of such a particle.

Ground-state cooling has been achieved for the center-of-mass motion of a 150 nm diameter SiO<sub>2</sub>-particle [5], and matter-wave interferometry has been demonstrated for a molecule with a mass of  $2.5 \times 10^4$  atomic mass units [6]. However, no ground-state cooling or quantum states have been demonstrated for particles in the micrometer scale, due to the larger amount of decoherence that comes with increasing size. Optical levitation is by far the most mature and successful levitation technique. However, it can levitate particles no larger than a few micrometers, because larger particles absorb enough laser power to melt and sublime [7]. Magnetic levitation provides advantages over optical levitation in that respect [8]. First, the trapping can be made completely passive by use of persistent currents, which removes the shot noise of lasers. Second, it is not limited in the particle size that can be levitated, so more massive systems are well within reach. And finally, a magnetically levitated particle can be coupled to superconducting circuits, which can be used to control the particle motion and achieve ground-state cooling [8].

### 1.2 Aim

In this thesis, the first aim is to compare the microwave properties of Al and Nb-based superconducting CPW resonators. Al is a type-I superconductor, for which  $T_C = 1.2$  K is well above the base temperature achieved in a dilution refrigerator. By fabricating Al-based CPW resonators, it would be possible to indirectly couple the resonators to the center-of-mass motion of the particle. Nb, a type-II superconductor, has both higher  $T_C$  and much higher first critical field than Al. This is of interest, as Nb CPW resonators could withstand magnetic fields that are used to

levitate the particle, without destroying superconductivity. This could open the possibility to couple directly to the center-of-mass motion of the particle. Furthermore, oxide-base Josephson junctions, fabricated from Al/Al<sub>2</sub>O<sub>3</sub>/Al are used to form DC SQUIDS, in order to embed these into Al-based CPW resonators. The Josephson inductance will change as magnetic flux ( $\Phi$ ) is threaded through the SQUIDS, thus modulating the resonance frequency of the CPW resonators. The second aim of the thesis is to characterize the flux tunability of SQUID-based Al CPW resonators, in order to determine  $\partial\omega/\partial\Phi$  of the single-photon coupling rate to the center-of-mass motion of the particle.

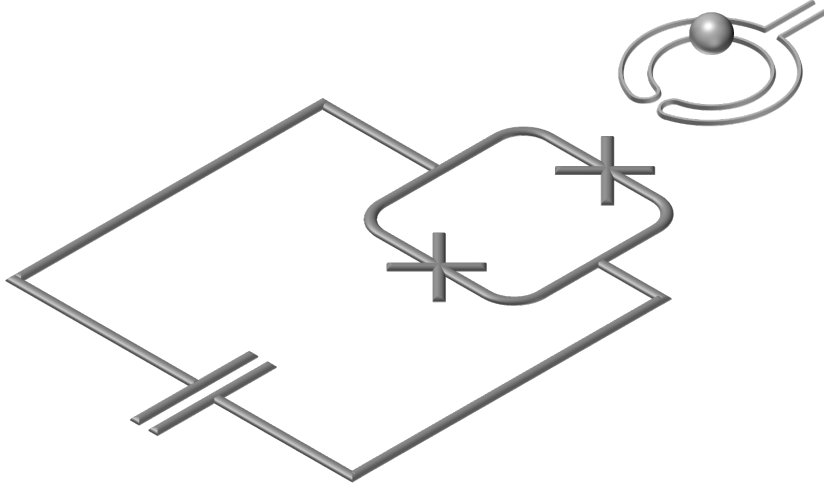


**Figure 1.1:** Schematic of the thesis aim, with a superconducting resonator circuit with an embedded SQUID, coupled to the levitating superconducting particle in a harmonic trap.

The thesis outline begins with Chapter 2 - Theory, in which the basics of superconductivity are presented, followed by a description of superconducting resonators. These two concepts are combined, to detail how flux-tunability can be used to modulate the resonance frequency. Lastly, superconducting levitation is presented, together with a brief introduction on two different coupling mechanisms. Chapter 3 - Methodology presents how the simulation of the superconducting resonators is set up. The cryostat used for the experiments is explained, alongside the measurement set-up. The device fabrication of both CPW and FTR is also presented in this chapter, followed by how the experimental procedure of the measurements are done. Chapter 4 - Results briefly presents measurements done to determine  $j_c$  of Al. The rest of the chapter is split into two halves: The first one showing the characterization of the CPW resonator, the latter half showing the attempt to modulate the frequency of SQUID-based Al CPW resonators through tuning the flux. The thesis is summarized in Chapter 5 - Conclusions, together with proposed future work.

# 2

## Theory

This chapter is divided into four sections: The first one will introduce the basic concepts of superconductivity and the physics of Josephson junctions and superconducting quantum interference devices (SQUIDs). The second will describe the physics, design and architecture of superconducting co-planar waveguide resonators. This is followed by the third section describing how flux tunability of a resonator is achieved by embedding a SQUID into it. Lastly, a description regarding levitation of a superconducting particle.

### 2.1 Superconductivity

Superconductivity appears as temperature falls below the critical temperature,  $T_C$ , which is different for each superconducting material [9]. As materials become superconducting, the electric resistance abruptly vanishes and magnetic fields are expelled from the interior of the material, behaving like a perfect diamagnet. In other words, the magnetic flux density  $\mathbf{B} = 0$  inside the material. This effect is known as the Meissner-Ochsenfeld effect, see Figure 2.1.

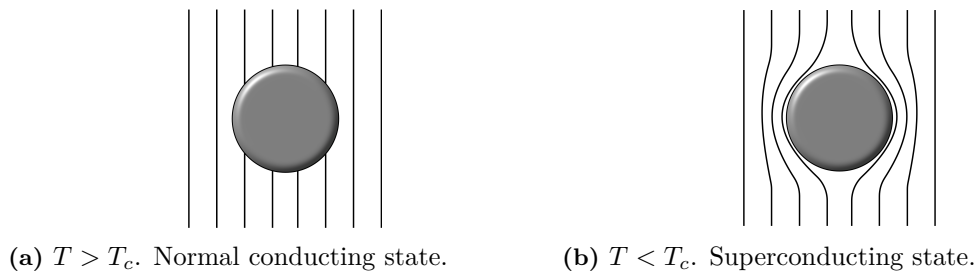


**Figure 2.1:** Illustration of the Meissner-Ochsenfeld effect of a superconducting sphere. (a) Magnetic flux threads through the sphere as  $T > T_c$ . (b) When cooled below  $T_c$ , magnetic flux is expelled from the superconductor.

There are two characteristic length scales for superconducting materials: The London penetration depth,  $\lambda_L$ , and the coherence length,  $\xi$  [9].  $\lambda_L$  describes the depth which an external magnetic field penetrates into a superconductor and decays by a factor of  $e^{-1}$ .  $\xi$  describes the average distance between two electrons that form a Cooper pair inside a superconductor.

Depending on whether  $\lambda/\xi$  is smaller or larger than  $1/\sqrt{2}$ , a superconductor is either of type-I or type-II, respectively [9]. In type-I superconductors the magnetization,  $\mathbf{M}$ , will oppose the applied magnetic field,  $\mathbf{H}$ , until it reaches the critical field,  $H_c$ . As  $H_c$  is reached, superconductivity abruptly disappears, see Figure 2.2a. Type-II superconductors also behave as type-I superconductors up to a critical field. However, the behavior of their magnetization differs from type-I superconductors. As the applied field increases up to a lower critical field,  $H_{c1}$ , the Meissner effect behaves just as a type-I superconductor. Between  $H_{c1}$  and the upper critical field,  $H_{c2}$ , however, magnetic flux penetrates into the superconductor in the form of magnetic flux vortices, called Abrikosov vortices. Superconductivity vanishes for fields larger than  $H_{c2}$ , see Figure 2.2b.

As a material transitions to its superconducting state, the electrons undergo a phase transition into Cooper pairs, and all pair-forming electrons are subsequently described by a single wave function [10]

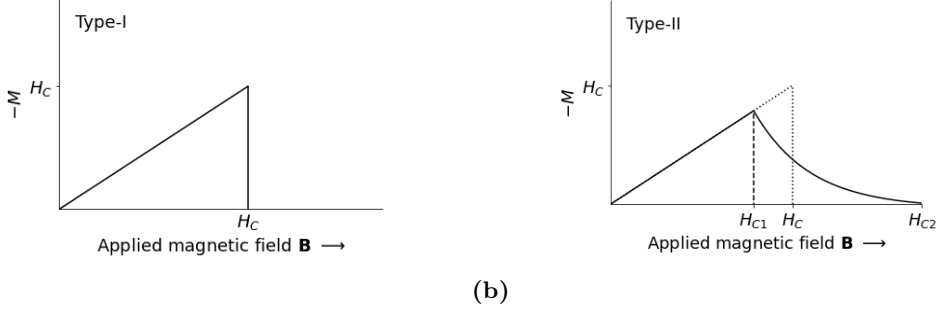


**Figure 2.2:** Magnetization versus applied magnetic field of (a) a type-I and (b) a type-II superconductor. (a) For type-I superconductors, the material becomes normal conducting when the applied magnetic field is higher than  $H_c$ . (b) For type-II superconductors, magnetic flux will penetrate the material if the applied magnetic field is higher than  $H_{c1}$ . The superconductor is in a vortex state between  $H_{c1}$  and  $H_{c2}$ . The material is normal conducting above  $H_{c2}$ . Dotted line is the response of an equivalent type-I material, shown for reference.

$$\psi = n^{1/2} e^{i\theta(\mathbf{r})}, \quad (2.1)$$

where  $n$  is the concentration of Cooper pairs and  $\theta(\mathbf{r})$  is the phase of the wave function. Given an applied magnetic vector potential  $\mathbf{A}$ , the velocity  $\mathbf{v}$  of the Cooper pairs can be described as

$$\mathbf{v} = m^{-1} (-i\hbar\nabla - q\mathbf{A}), \quad (2.2)$$

where  $m$  and  $q$  are the mass and charge of a single Cooper pair, respectively, and  $\hbar$  is the reduced Planck constant. This gives an expression for the electric current density with the form

$$\mathbf{j} = q\psi^* \mathbf{v}\psi = \frac{nq}{m} (\hbar\nabla\theta - q\mathbf{A}). \quad (2.3)$$

It is observed that  $\mathbf{j}$  is obtained from the probability density of the wave function. Equation (2.3) describes the flow of electric current that arises from Cooper pairs under a magnetic field. When looking at a superconducting loop, a current can be induced within it by applying a magnetic flux on the area enclosed by the ring. However, well inside the superconducting ring,  $\mathbf{j}$  is zero due to the Meissner-Ochsenfeld effect. Integrating  $\mathbf{j}$  along a closed path,  $C$ , inside the ring yields

$$\frac{nq}{m} \left( \hbar \oint_C \nabla\theta \cdot d\mathbf{l} - q \oint_C \mathbf{A} \cdot d\mathbf{l} \right) = 0, \quad (2.4)$$

where  $d\mathbf{l}$  is a line element of the ring. The integral of the phase gradient gives the phase change ( $\theta_2 - \theta_1$ ) accumulated over one full revolution around the ring. Due to the wave function being continuous inside the entire ring, the phase difference must equal  $2\pi n$ , where  $n$  is an integer, otherwise the wave function would be discontinuous. Then, the integration of  $\mathbf{A}$  becomes

$$\oint_C \mathbf{A} \cdot d\mathbf{l} = \int_C \nabla \times \mathbf{A} \cdot d\boldsymbol{\sigma} = \int \mathbf{B} \cdot d\boldsymbol{\sigma} = \Phi \quad (2.5)$$

where  $d\boldsymbol{\sigma}$  is the area enclosed by the ring. Thus, Equation (2.4) can be rewritten as

$$\frac{nq}{m} (2\pi\hbar n - q\Phi) = 0 \implies \Phi = \frac{2\pi\hbar}{q} n. \quad (2.6)$$

Thus, the magnetic flux  $\Phi$  through a superconducting loop is quantized in multiples of  $2\pi\hbar/q$ , the magnetic flux quantum ( $\Phi_0$ )

$$\Phi_0 = \frac{h}{2e} \approx 2.067\ 833\dots \times 10^{-15} \text{ Wb}. \quad (2.7)$$

### 2.1.1 Josephson Junctions

Whenever two superconductors are separated by an insulator, such as an oxide layer, which is shorter than the coherence length of the superconductors, Cooper pairs will tunnel through the insulator. This phenomenon is known as Josephson tunneling [9], which is the foundation of the DC-Josephson effect. In the DC Josephson effect, electric current flows through an SIS (superconductor-insulator-superconductor) junction in the absence of any electric or magnetic field. The DC current,  $I$ , across a junction depends on the phase difference between the Cooper pair wave functions at the two sides of the junction, according to

$$I = I_c \sin(\Delta\theta), \quad \Delta\theta = \theta_2 - \theta_1, \quad (2.8)$$

where  $\theta_1$  and  $\theta_2$  denote the phase in the superconductor before and after the junction, respectively, see Figure 2.3. The critical current,  $I_c$ , is the maximum current that can be passed through a Josephson junction (JJ) at zero-voltage.



**Figure 2.3:** Schematics of a SIS junction. **(left)** The phase difference changes as wavefunction of the Cooper pairs tunnel through the junction. **(right)** The Cooper-pair density distribution around the junction.

### 2.1.2 RF & DC SQUID

A superconducting quantum interference device (SQUID) is a superconducting loop containing at least one JJ. SQUIDs are categorized into two types depending on the number of JJs: RF and DC SQUIDs, which contain one and two JJs respectively, see Figure 2.4.

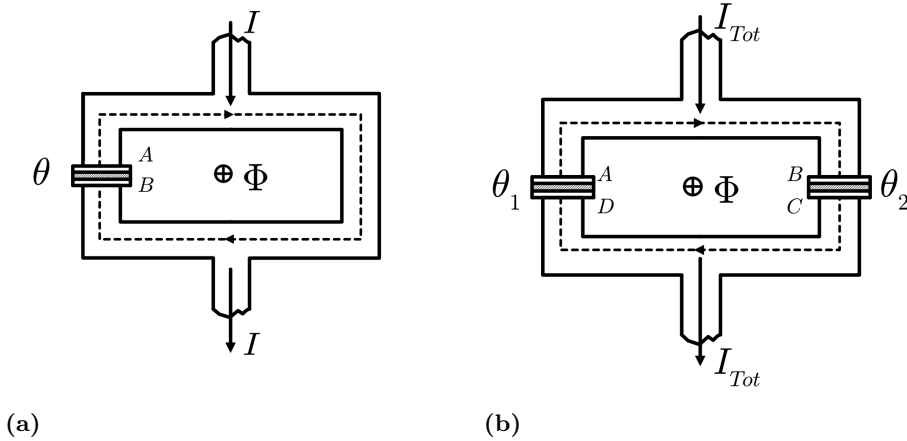


**Figure 2.4:** Schematics of an (a) RF SQUID and (b) DC SQUID with an applied current.

By integrating Equation (2.3) along the dashed line in an RF SQUID depicted in Figure 2.4a, where  $\mathbf{j}$  is zero, from A to B excluding the gap, the phase gradient will be expressed as

$$\hbar \int_B^A \nabla\theta \cdot d\mathbf{l} = \hbar \left( \oint \nabla\theta \cdot d\mathbf{l} - \int_A^B \nabla\theta \cdot d\mathbf{l} \right) = -2e \left( \oint \mathbf{A} \cdot d\mathbf{l} + \int_A^B \mathbf{A} \cdot d\mathbf{l} \right), \quad (2.9)$$

since  $\hbar\nabla\theta = -2e\mathbf{A}$ , that is, the change in phase is proportional to the applied magnetic field. For revolutions along a closed path  $\nabla\theta = 2\pi n$ . From Equation (2.5), it is known that the closed

integral of  $\mathbf{A}$  is equal to the magnetic flux threading the area enclosed by the superconducting loop, such that (2.9) will express as

$$2\pi n + (\theta_A - \theta_B) = -\frac{2\pi\Phi}{\Phi_0} - \frac{2e}{\hbar} \int_A^B \mathbf{A} \cdot d\mathbf{l}. \quad (2.10)$$

If we choose the gauge for  $\mathbf{A}$  such that the integral  $\int_A^B \mathbf{A}$  is zero (which does not change the system because  $\mathbf{A}$  is gauge invariant), the phase difference  $\theta = \theta_A - \theta_B$  will be [11]

$$\theta = 2\pi n - \frac{2\pi\Phi}{\Phi_0}. \quad (2.11)$$

Thus, the current in an RF SQUID becomes

$$I = I_c \sin(\theta) = I_c \sin\left(2\pi n - 2\pi \frac{\Phi}{\Phi_0}\right) = -I_c \sin\left(2\pi \frac{\Phi}{\Phi_0}\right). \quad (2.12)$$

If an external magnetic flux,  $\Phi_{\text{ext}}$ , is applied, the total flux  $\Phi$  threading the superconducting loop will be the sum of  $\Phi_{\text{ext}}$  and a self-induced flux created by the current circulating inside the SQUID, expressed as

$$\Phi = \Phi_{\text{ext}} + LI. \quad (2.13)$$

Substituting Equation (2.13) into (2.12), yields the current that circulates inside the SQUID

$$I = -I_c \sin\left[2\pi \frac{\Phi_{\text{ext}}}{\Phi_0} + \beta_L \frac{I}{I_c}\right] \quad (2.14)$$

where  $\beta_L$  is the screening parameter defined as

$$\beta_L = 2\pi \frac{LI_c}{\Phi_0}. \quad (2.15)$$

If Equation (2.12) is substituted into (2.13), the magnetic flux in the SQUID would be expressed as a function of externally applied flux:

$$\frac{\Phi}{\Phi_0} = \frac{\Phi_{\text{ext}}}{\Phi_0} - \frac{\beta_L}{2\pi} \sin\left(\frac{2\pi\Phi}{\Phi_0}\right). \quad (2.16)$$

Equation (2.16) describes how the flux inside the SQUID-loop behaves in terms of the externally applied flux. Note that the equation is self-consistent, and only if  $\beta \leq 1$  will it yield single-valued results. However, if  $\beta > 1$ , (2.16) it will become a multiple-valued function, which will lead to hysteretic behavior, see Figure 2.5.

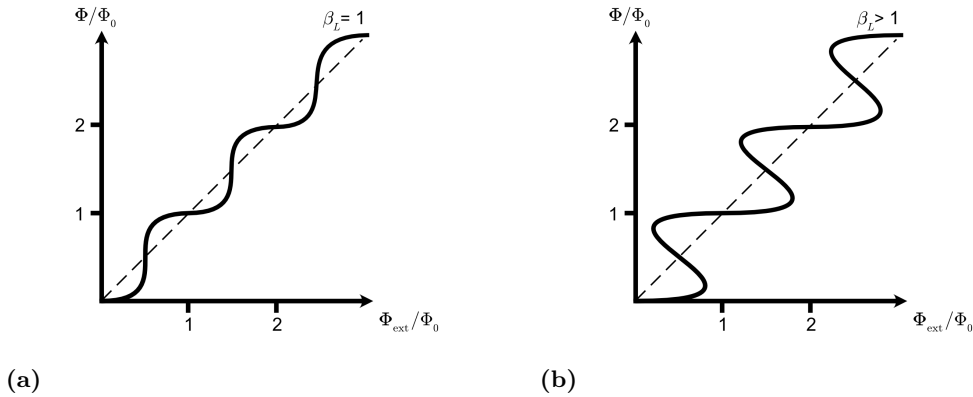


**Figure 2.5:**  $\Phi$  as a function of  $\Phi_{\text{ext}}$  for (a)  $\beta_L = 1$  and (b)  $\beta_L > 1$ , where the hysteretic behavior appears.

Due to the multiple-valued property from the hysteretic behavior, it becomes impossible to determine how applied flux affects the flux inside the SQUID-loop. Hysteresis in SQUIDS are thus undesired, as they will be inoperable.

When there are two JJs in a superconducting loop, the Cooper pair wave function starts interfering with itself [11]. The phase at the JJs for a DC SQUID can be derived in the same way as for the RF SQUID case. The total current deep within the superconducting loop is zero, such that the integral of the phase around the loop, excluding the junction gaps, becomes

$$\oint \nabla \theta \cdot d\mathbf{l} - (\theta_D - \theta_A) - (\theta_C - \theta_B) = -\frac{2e}{\hbar} \left( \oint \mathbf{A} \cdot d\mathbf{l} - \int_B^A \mathbf{A} \cdot d\mathbf{l} - \int_D^C \mathbf{A} \cdot d\mathbf{l} \right). \quad (2.17)$$

Evaluating (2.17) similarly as in Equation (2.10) leads to

$$\theta_2 = \theta_1 - 2\pi \frac{\Phi}{\Phi_0}, \quad (2.18)$$

with  $\theta_1$  and  $\theta_2$  being the phase difference across each junction.  $\Phi$  is pointing inwards in Figure 2.4b, just like for the RF SQUID. If we assume that the JJs are symmetric, it follows that  $I_{C1} = I_{C2} = I_C$  and the DC Josephson effect would then be expressed as

$$I_{Tot} = I_1 + I_2 = I_{C1} \sin(\theta_1) + I_{C2} \sin(\theta_2) = I_C (\sin(\theta_1) + \sin(\theta_2)). \quad (2.19)$$

Plugging in Equation (2.18) into (2.19) it is found that

$$\begin{aligned} I_{Tot} &= -2I_C \sin\left(\frac{\theta_1 + \theta_2}{2}\right) \cos\left(\frac{\theta_1 - \theta_2}{2}\right) \\ &= -2I_C \sin\left(\theta_1 + \pi \frac{\Phi}{\Phi_0}\right) \cos\left(\pi \frac{\Phi}{\Phi_0}\right) \end{aligned} \quad (2.20)$$

The sine-term is phase dependent, while the cosine-term is solely dependent on the magnetic flux. Maximizing Equation (2.20) with respect to  $\theta_1$  yields the maximum value for the critical current of the JJs, denoted  $I_M$ :

$$|I_M(\Phi)| = 2I_C \left| \cos\left(\pi \frac{\Phi}{\Phi_0}\right) \right|. \quad (2.21)$$

Equation (2.21) is valid under the assumptions that the JJs are symmetric and that no flux is self-induced in the SQUID-loop. Assuming  $\Phi = \Phi_{\text{ext}}$  yields a relation of how the current in the loop is affected by externally applied fields, see Figure 2.6. It can be seen that for integer values of  $\Phi_0$ ,  $I_M$  will reach its highest values. This current modulation can be used to modulate the frequency of a SQUID-cavity, see Section 2.3.

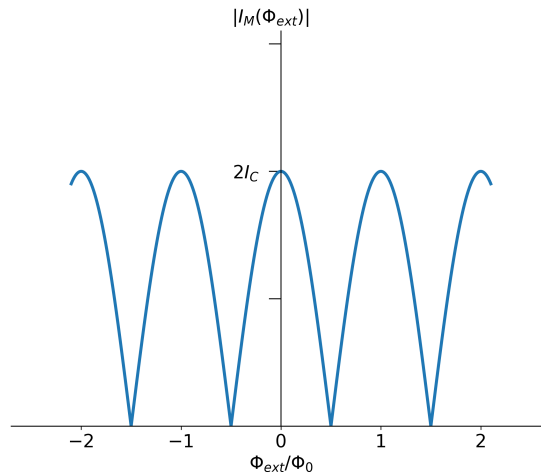


**Figure 2.6:**  $|I_M|$  as a function of  $\Phi_{\text{ext}}/\Phi_0$ .  $I_M$  reaches peak values at integer values of  $\Phi_{\text{ext}}/\Phi_0$

## 2.2 Superconducting Resonators

In this section, the physics of superconducting co-planar waveguide resonators is discussed. Scattering parameters for a feedline and resonator will be explained through the concept of impedance and the ratio of the impedance of these two components. Furthermore, quality factors are introduced as a measure of loss of a resonant circuit and will play a central role for superconducting CPW resonators. Lastly, an expression for the number of intra-cavity photons in a resonator will be derived.

### 2.2.1 Co-planar waveguide resonators

A co-planar waveguide (CPW) is formed by a central conductor of width  $W$ , separated from the ground plane on either side by a width  $S$ , made from the same superconducting material, standing on a non-conducting substrate [12], see Figure 2.7

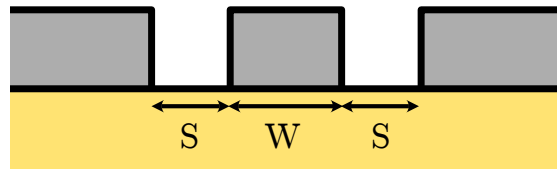


**Figure 2.7:** Cross-section of a co-planar waveguide. The central conductor, of width  $W$ , is separated from the ground plane on either side by a width  $S$ . The substrate is illustrated as yellow and the superconductor as gray.

All CPW resonators have a resonance frequency,  $\omega_0$ , given by

$$\omega_0 = \frac{c}{\sqrt{\epsilon_{eff}}} \frac{2\pi}{\lambda_0}, \quad (2.22)$$

where  $c$  is the speed of light and  $\lambda_0$  is the wavelength of the fundamental mode of the resonator.  $\epsilon_{eff}$  is the effective permittivity given by  $\epsilon_{eff} = (\epsilon_1 + \epsilon_2)/2$ , where  $\epsilon_1 \approx 1$  for air and  $\epsilon_2 = 11.6$  is the relative permittivity of the Si-substrate [13], assuming that the electric field penetration is 50 % in air and 50 % in the substrate respectively, in Figure 2.7.  $c/\sqrt{\epsilon_{eff}}$  is the phase velocity,  $\nu_p$ , of the electromagnetic waves propagating along the CPW. Thus,  $\nu_p$  depends on the material properties according to

$$\nu_p = \frac{1}{\sqrt{LC}} \quad (2.23)$$

where  $L$  and  $C$  are the inductance and capacitance per unit length, respectively. Using conformal mapping, it is possible to express  $L$  and  $C$  as [14], [15]

$$L = \frac{\mu_0}{4} \frac{K(k')}{K(k)}, \quad C = 4\epsilon_0\epsilon_{eff} \frac{K(k)}{K(k')} \quad (2.24)$$

where  $\mu_0$  and  $\epsilon_0$  are the permeability and the permittivity of vacuum, respectively.  $K$  is the complete elliptic integral of the first kind, in which the geometric arguments  $k$  and  $k'$  are described as

$$k = \frac{W}{W + 2S}, \quad k' = \sqrt{1 - k^2}. \quad (2.25)$$

$\omega_0$  will thus depend on the geometry of the CPW, as

$$\omega_0 = \frac{2\pi}{\lambda_0 \sqrt{LC}}. \quad (2.26)$$

### 2.2.2 Transmission line impedance

The characteristic impedance of a transmission line is a complex number, which can be derived from the telegrapher equation [16]

$$Z_0 = \sqrt{\frac{R + i\omega L}{G + i\omega C}}, \quad (2.27)$$

with  $R$  as the resistance per unit length of the transmission line,  $G$  the conductance of the dielectric per unit length, and  $L$  and  $C$  inductance and capacitance per unit length. In this expression, the real numbers correspond to the losses of the circuit.

The complex propagation constant,  $\gamma$ , of the electromagnetic wave in the system is expressed as

$$\gamma = \sqrt{(R + i\omega L)(G + i\omega C)} = \alpha + i\beta \quad (2.28)$$

where  $\alpha$  and  $\beta$  are the attenuation and propagation constants, respectively.

When considering a system with near zero losses, the characteristic impedance can be approximated to

$$Z_0 \simeq \sqrt{\frac{L}{C}}. \quad (2.29)$$

Transmission lines are usually designed such that  $Z_0$  is 50  $\Omega$ , which is the optimal trade-off impedance between loss and maximum power transfer for coaxial cables [17]. For a low loss case,  $Z_0$  depends on  $L$  and  $C$ , which are mostly determined by geometric quantities.  $\alpha$  and  $\beta$  become

$$\alpha \simeq \frac{1}{2} \left( \frac{R}{Z_0} + GZ_0 \right), \quad \beta \simeq \omega\sqrt{LC} = \omega/\nu, \quad (2.30)$$

where  $\nu$  is the phase velocity of electromagnetic waves in the transmission line.  $\alpha$  is a measure of attenuation inside the transmission line, due to conductor, dielectric or radiation losses [16].  $\beta$  describes the wave propagation inside the transmission line. The overall loss of the transmission line is measured by the unloaded quality factor,  $Q_i$ , which is the ratio of the energy stored inside the transmission line to the power lost over one period:

$$Q_i = \omega \frac{\text{average energy stored}}{\text{energy loss/second}} = \frac{\beta}{2\alpha}. \quad (2.31)$$

Therefore, for low losses,  $Q_i$  will be higher. The index  $i$  stands for internal quality factor of a transmission line.

### 2.2.3 Quarter-wave resonators

A quarter-wave resonator is a CPW in which one end, closest to the feedline, is kept open, and the other is grounded, that is, terminated with zero load. Quarter-wave resonators are preferred over half-wave resonators in this project, as the elbow coupling is easier to design (see Figure 2.8 compared to the finger design in a half-wave resonator [12]). Additionally, the current is the highest at the ground-end, which is relevant when designing flux-tunable resonators, see Section 2.3. The impedance,  $Z_{\text{TLR}}$ , for such a resonator in terms of  $Z_0$ , is expressed as follows [16].

$$Z_{\text{TLR}} = Z_0 \tanh(\gamma l) = Z_0 \frac{1 - i \tanh(\alpha l) \cot(\beta l)}{\tanh(\alpha l) - i \cot(\beta l)}, \quad (2.32)$$

where  $l$  is the length of the resonator.

For unloaded quarter-wave resonators (i.e. disconnected from the environment), the resonance frequency is  $\omega_{1/4}$ . The detuning, that is, the difference between probing frequency and  $\omega_{1/4}$ , is defined as

$$\delta\omega_{1/4} = \omega - \omega_{1/4}. \quad (2.33)$$

At near resonance,  $\delta\omega_{1/4} \sim 0$ , Eq. (2.32) simplifies to

$$Z_{\text{TLR}} = Z_0 \frac{\frac{4Q_i}{\pi} - i \frac{8Q_i^2}{\pi} \frac{\delta\omega_{1/4}}{\omega_{1/4}}}{1 + 4Q_i^2 \left( \frac{\delta\omega_{1/4}}{\omega_{1/4}} \right)^2}. \quad (2.34)$$

A resonator can be coupled capacitively to a feedline, see Figure 2.8.

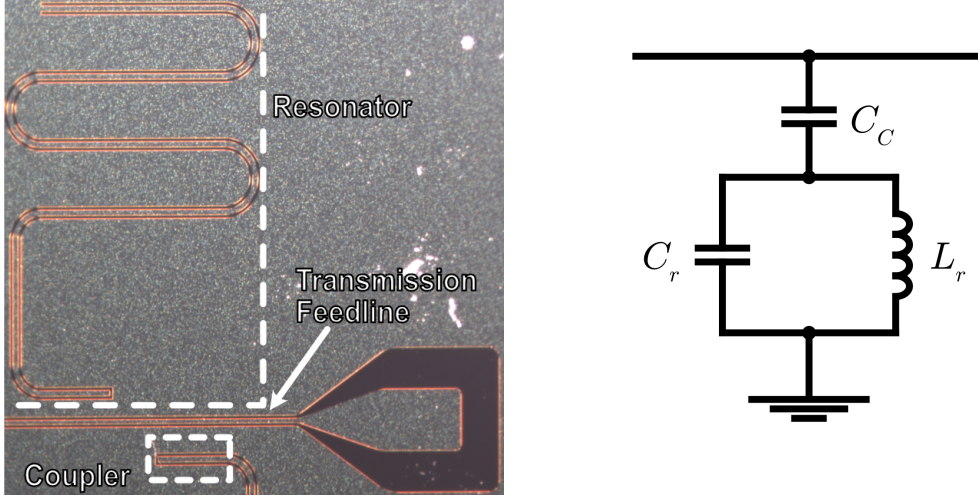


**Figure 2.8:** (left) A meandered quarter-wave CPW resonator. One end is capacitively coupled to the feedline and the other end is shorted to ground. The central conductor for the resonator and transmission line have the same width and spacing between the central conductor and ground plane. (right) Schematic of the equivalent circuit of a resonator coupled to a feedline.

The total impedance of the resonant circuit,  $Z$ , is thus expressed as

$$Z = Z_{\text{TLR}} - i \frac{1}{\omega C_C}, \quad (2.35)$$

where  $C_C$  is the total capacitance between the resonator and the feedline, see schematic in Figure 2.8. Note that the impedance of a loaded resonator (i.e. a resonator coupled to a feedline) depends on the inductance and capacitance of the CPW resonator. By changing the geometric dimensions of the resonator, such as the central conductor width, spacing between the central conductor and ground plane, length of the coupler or the meandered regions of the resonator, the capacitance and inductance can be modified.  $Z$  can thus be matched to  $Z_0$  in order to maximize the transmission from feedline to resonator.

The average energy stored in the resonator is given by its inductance and capacitance. As electromagnetic waves travel through the resonator, the average energy stored capacitively in the meandering of the resonator expresses as

$$E_C = \frac{1}{2} C_r \langle V^2 \rangle, \quad (2.36)$$

where  $C_r$  is the total capacitance in the resonator and  $\langle V^2 \rangle$  is the mean square voltage.  $C_r$  can be calculated as

$$C_r = Cl = \frac{l}{\nu Z_0} = \frac{2\pi l}{\omega \lambda Z_0} = \frac{\pi}{2\omega Z_0} \quad (2.37)$$

where  $l$  is the resonator length,  $\nu = \omega\lambda/2\pi$  and  $\lambda$  is the wavelength. In this calculation, the fundamental frequency is defined as  $\lambda = 4l$ , for a quarter-wave resonator. The power that is transmitted between feedline and resonator is found through

$$P = \langle I^2 \rangle Z_0 = \langle (\omega C_C V)^2 \rangle Z_0. \quad (2.38)$$

The ratio between the incoming energy in the feedline per cycle and the energy stored in the resonator is quantified by the external quality factor, known here as the coupling quality factor,

$Q_C$ . Taking the average energy stored inductively in the resonator into account, results in doubling of the energy  $E = 2E_C$ , such that  $E$  and  $P$  can be substituted in to the definition of quality factors, see Equation (2.31):

$$Q_C = \omega \frac{E}{P} \quad (2.39)$$

$$Q_C = \omega \frac{1}{2} \frac{\langle V^2 \rangle \pi}{Z_0^2 \langle (\omega C_C V)^2 \rangle} = \frac{\pi}{2Z_0^2 \omega C_C^2}. \quad (2.40)$$

It is now possible to determine the total impedance by plugging Equations (2.34) and (2.40) in (2.35) such that  $Z$  is

$$\frac{Z}{Z_0} = \frac{\frac{4Q_i}{\pi} - i \frac{8Q_i^2}{\pi} \frac{\delta\omega_{1/4}}{\omega_{1/4}} - i \sqrt{\frac{2Q_C}{\pi}} \left[ 1 + 4Q_i^2 \left( \frac{\delta\omega_{1/4}}{\omega_{1/4}} \right)^2 \right]}{1 + 4Q_i^2 \left( \frac{\delta\omega_{1/4}}{\omega_{1/4}} \right)^2}. \quad (2.41)$$

By definition, the imaginary part of Equation (2.41) is zero at resonance [16]. Solving  $\text{Im}(Z) = 0$  for  $\delta\omega_{1/4}/\omega_{1/4}$ , the normalized detuned resonance frequency can be determined to  $\delta\omega_{1/4}/\omega_{1/4} = -\sqrt{2}/(\pi Q_C)$ . Since a load is added by capacitively coupling the feedline and the resonator, the resonance frequency of the loaded CPW resonator,  $\omega_0$ , will be lower than the unloaded resonance frequency  $\omega_0 < \omega_{1/4}$ .  $\omega_0$ , defined in Equation (2.22), can be expressed as

$$\omega_0 = \frac{2\pi}{\sqrt{L_r C_r}} \quad (2.42)$$

$$L_r = \frac{8l}{\pi^2} L, \quad C_r = \frac{1}{2} Cl$$

where  $L_r$  and  $C_r$  are the total inductance and capacitance of the resonator coupled to a feedline, respectively. The pre-factors for  $L_r$  and  $C_r$  account for the electric field distribution inside the CPW resonator [12]. The normalized detuned resonance frequency will thus be redefined as  $\delta\omega_{1/4}/\omega_{1/4} = \delta\omega_0/\omega_0 - \sqrt{2}/(\pi Q_C)$ , where  $\delta\omega_0 = \omega - \omega_0$ . For a loaded CPW resonator at near resonance where  $\delta\omega_0 \sim 0$ , Equation (2.41) will be expressed in terms of  $\omega_0$  according to

$$\frac{Z}{Z_0} = \sqrt{\frac{2Q_C}{\pi}} \frac{2Q_i \frac{\delta\omega_0}{\omega_0} - i}{1 + i2Q_i \frac{\delta\omega_0}{\omega_0} - i2Q_i \sqrt{\frac{2}{\pi Q_C}}}. \quad (2.43)$$

Equation (2.43) quantifies the impedance mismatch. In an ideal case,  $Z = Z_0 = 50 \Omega$  such that the transmission between the two lines is maximum.

## 2.2.4 Scattering parameters

The input and output of a feedline can be modelled as a two-port network. The transmission and reflection of the traveling waves in the feedline can be expressed through the scattering matrix  $[\mathbf{S}]$ :

$$[\mathbf{S}] = \begin{pmatrix} S_{11} & S_{12} \\ S_{21} & S_{22} \end{pmatrix}, \quad (2.44)$$

where the indices signify ports 1 (feedline input) and 2 (feedline output). Expressing the two-port network in terms of impedance, the scattering from ports 1 to 2,  $S_{21}$ , is generally expressed as [16]

$$S_{21} = \frac{2Z_{12}Z_0}{(Z_{11} + Z_0)(Z_{22} + Z_0) - Z_{12}Z_{21}}. \quad (2.45)$$

Assuming that the impedance of the feedline and the ports are the same, that is  $Z_{i,j} = Z$ ,  $S_{21}$  can be simplified to

$$S_{21} = \frac{2}{2 + \frac{Z_0}{Z}} \quad (2.46)$$

which is the same as for  $S_{12}$ . Using Equation (2.43), it is found that  $S_{21}$  at resonance will yield

$$S_{21}(\omega_0) = \frac{Q_C}{Q_C + Q_i}. \quad (2.47)$$

The loaded quality factor is a reciprocal sum of the external and unloaded factors:

$$\frac{1}{Q_l} = \frac{1}{Q_C} + \frac{1}{Q_i}. \quad (2.48)$$

Thus, it is possible to express the scattering parameter from ports 1 and 2 at near resonance in terms of quality factors:

$$S_{21} = \frac{S_{21}(\omega_0) + i2Q_l \frac{\delta\omega_0}{\omega_0}}{1 + i2Q_l \frac{\delta\omega_0}{\omega_0}}. \quad (2.49)$$

This expression quantifies the transmission coefficient of a propagating wave in the feedline past the resonator [18], see Figure 2.9.

A resonator circuit coupled to a feedline can be represented as a three-port network, shown in Figure 2.9, which illustrates the feedline input and output ports as 1 and 2 respectively, while the resonator is represented as port 3. The arrows indicate the directions of the scattering.

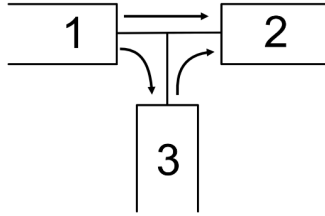


**Figure 2.9:** Network representation of the feedline in- (1) and out-port (2), as well as the resonator (3). The scattering is also depicted.

The scattering matrix for the three-port network is 3-dimensional [16]. In this network representation, the scattering parameters  $S_{21} = S_{12}$  as they quantify the transmission between port 1 and 2. Because the three-port network is reciprocal  $S_{31} = S_{13}$  and  $S_{32} = S_{23}$ . The dimensions of the coupler are assumed to be much smaller than the wavelength, resulting in the ports 1 and 2 appearing symmetric in relation to port 3, such that  $S_{13} = S_{23} = S_{31} = S_{32}$ . It is possible to express the power leaked from port 3 into port 1 and 2 as [19]

$$P = 2fE(|S_{13}|^2 + |S_{23}|^2) \quad (2.50)$$

Substituting (2.50) into the definition of the coupling quality factor, see Equation (2.39), results in  $Q_C$  as an expression of the scattering parameters [19]

$$Q_C = \omega \frac{E}{P} = \frac{\pi}{2|S_{13}|^2}, \quad (2.51)$$

under the assumption  $S_{13} = S_{23}$ .

### 2.2.5 Resonance Circles and model fit

The resonator circuit and scattering parameters describe an ideal resonator. Non-ideal resonators account for impedance mismatches between the impedance of the feedline and the resonator. Additionally, resonator coupling is a combination of both capacitive and inductive coupling, which results in more complex behavior. A generalized resonator model has been proposed in [20], where  $Q_C$  is expressed as a complex coupling quality factor,  $Q_C = |Q_C| \exp(-i\phi)$ , taking both inductive and capacitive coupling into account.  $\phi$  quantifies impedance mismatches between the feedline and the resonator. This model is expressed the scattering parameter  $S_{21}$  as [21]

$$S_{21}^{\text{model}} = ae^{i\alpha}e^{-i\omega\tau} \left[ 1 - \frac{(Q_l/|Q_C|)e^{i\phi}}{1 + 2iQ_l\frac{\delta\omega_0}{\omega_0}} \right]. \quad (2.52)$$

where  $a$  and  $\alpha$  signify the background amplitude and phase shift, respectively, which originate from losses caused by the environment and electric cabling connected to the measurement instruments.  $\tau$  is the electric propagation delay coming from the same cabling. All contribute to non-ideal behavior of the system.

This is illustrated in Figure 2.10, for two example resonators with similar parameters ( $Q_l = 15\,000$ ,  $|Q_C| = 20\,000$ ,  $\omega_0 = 2\pi \times 6$  GHz). In Figure 2.10, the graphs on the left show magnitude and phase response of  $|S_{21}|$  as a function of probing frequency for ideal and non-ideal resonators (top and bottom, respectively). The abrupt change in  $|S_{21}|$  and  $\angle S_{21}$  as the probing frequency reaches resonance,  $\omega = \omega_0$ , is caused by absorption of photons into the resonator.

The graphs on the right are resonance circles of the  $S_{21}$  transmission, with the imaginary component as a function of the real component. A symmetric circle is formed for the ideal resonator in the magnitude and phase response because of the perfect impedance match. For the non-ideal case, the circle is heavily distorted due to significant impedance mismatch and attenuation. Experimental data is fitted with a fit routine [21] based on Equation (2.52). In this routine, imaginary and real parts of  $S_{21}$  data are fitted to this model, from which the impedance mismatch, resonance frequency and quality factors of the resonator can be extracted.

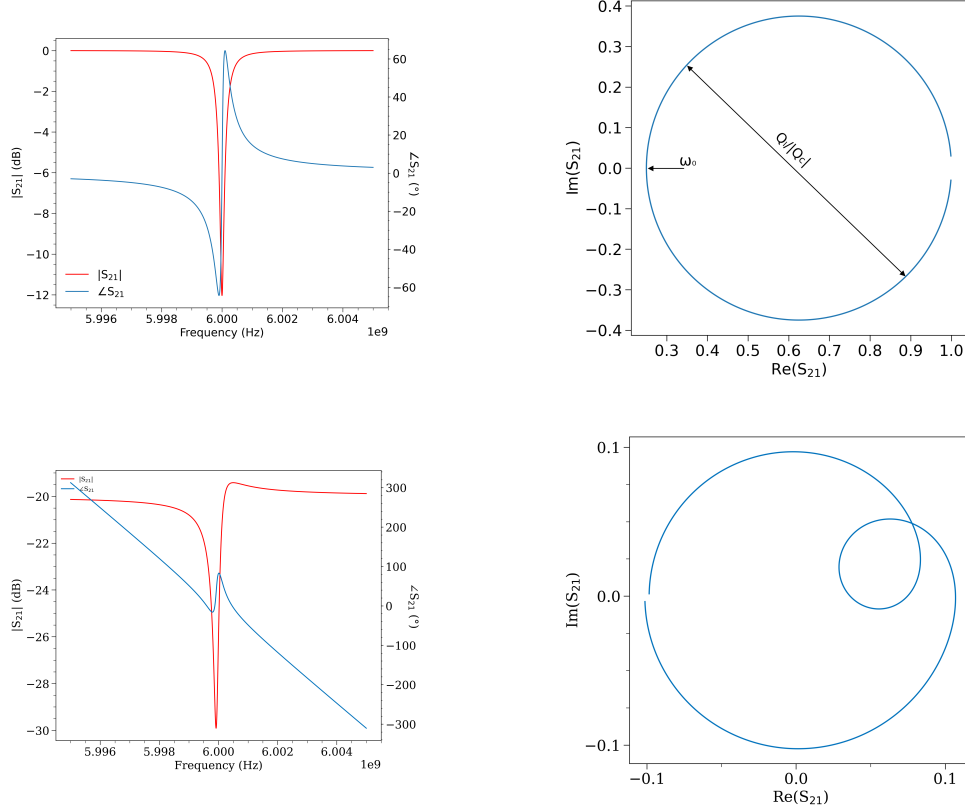


**Figure 2.10: (top)** Scattering magnitude and phase response for an ideal resonator, along with the resonance circle. The diameter of the circle is determined by the quality factor ratio  $Q_i/|Q_c|$  and the resonance frequency corresponds to the point where  $\text{Im}(S_{21}) = 0$  (Model parameters:  $\tau = 0$  ns,  $\phi = 0$ ,  $a = 1$ ,  $\alpha = 0$ ). **(bottom)** The response data and circle are skewed due to environmental damping effects. Impedance mismatch results in an asymmetry of the resonance dip in the  $|S_{21}|$  curve, while the resonance circle distortion is caused by the electric delay from the cabling (Model parameters:  $\tau = 100$  ns,  $\phi = -0.5$ ,  $a = 0.1$ ,  $\alpha = 0.01$ ).

### 2.2.6 Derivation of intra-cavity Photon number

Figure 2.9 shows how the scattering of the ports. Back-scattering is assumed to be low enough such that a negligible amount of photons is transmitted backwards (from right to left in the schematic). Thus, the signal at port 2 will be an expression of the waves coming from ports 1 and 3. This signal can be described in terms of voltages and scattering parameters as

$$V_1 = V_1 S_{21} + V_1 S_{31} + V_3 S_{23} \implies V_1 S_{21} = V_1(1 - S_{31}) - V_3 S_{23}, \quad (2.53)$$

in which  $V_1$  and  $V_3$  are the voltages at ports 1 and 3 respectively.

The ratio of power incident from feedline to resonator,  $P_{in}$  and power inside the resonator  $P_r$  is:

$$\frac{P_r}{P_{in}} = \frac{V_3^2/Z}{V_1^2/Z_0}, \quad (2.54)$$

where  $Z$  and  $Z_0$  are the impedance of the resonator and feedline, respectively. The ratio  $V_3/V_1$  is found from Equation (2.53), where at resonance, the scattering parameters are described from Equations 2.47 and 2.51. Thus, the ratio will be expressed in terms of the quality factors:

$$\frac{V_3}{V_1} = \frac{Q_i}{Q_c} \sqrt{\frac{2Q_c}{\pi}} - 1. \quad (2.55)$$

Assuming that the system is critically coupled, that is  $Q_i = Q_c$ , the ratio of voltage amplitudes between the two ports approximates to

$$\left(\frac{V_3^2}{V_1^2}\right) \approx \frac{2 Q_l^2}{\pi Q_c}. \quad (2.56)$$

Plugging the voltage ratios into Equation (2.54) gives

$$\frac{P_r}{P_{in}} = \frac{V_3^2/Z}{V_1^2/Z_0} = \frac{2 Q_l^2 Z_0}{\pi Q_c Z} \quad (2.57)$$

It is possible to express  $P_r$ , assuming the resonator is driven at resonance, in terms of the average energy multiplied by the resonance frequency. Together with Equation (2.57) it is found that

$$P_r = \omega_0 \langle E_r \rangle \implies \langle E_r \rangle = \frac{P_r}{\omega_0} = \frac{2 Q_l^2 Z_0}{\pi Q_c Z} \frac{P_{in}}{\omega_0}. \quad (2.58)$$

The average number of photons inside the resonator can be determined through dividing Equation (2.58) by  $\hbar\omega_0$

$$\langle n_p \rangle = \frac{\langle E_r \rangle}{\hbar\omega_0} = \frac{2Z_0 Q_l^2}{\pi Z Q_c \hbar\omega_0^2} P_{in}. \quad (2.59)$$

This equation makes the following assumptions: the resonator is driven at resonance and critically coupled. Furthermore, it is to be noted that  $P_{in}$  is the power incident from feedline to resonator.

### 2.3 Flux-tunable resonator

Embedding a DC SQUID into a superconducting quarter-wave CPW resonator enables tuning of the resonance frequency of the resonator via an externally applied flux. This can, for example, be used to detect and measure motion of mechanical resonators that generate magnetic signals on the SQUID through flux-coupling. In this section, the physics and function of flux tunable resonators are discussed.

In a quarter-wave superconducting CPW resonator, the current wave anti-node of the modes is found at the point where the resonator is grounded. Combining a SQUID and CPW resonator, by embedding the SQUID at this anti-node, forms a flux-tunable resonator (FTR) and enables modulation of the resonance frequency of the resonator by tuning  $\Phi_{\text{ext}}$  of the SQUID loop. The normalized eigenfrequency  $\omega_c/\omega_0$  of a FTR is determined by solving a dispersion equation [22]

$$\frac{\pi\omega_c}{2\omega_0} \tan\left(\frac{\pi\omega_c}{2\omega_0}\right) = \frac{(2\pi)^2}{\Phi_0^2} L_r E_s(\Phi_{\text{ext}}) \quad (2.60)$$

with  $\omega_0$  being the resonance frequency of the resonator without the SQUID and  $L_r$  the total inductance of the CPW resonator.  $E_s$  is the flux dependent energy of a DC-SQUID [23], determined by

$$E_s(\Phi_{\text{ext}}) = \frac{\Phi_0^2}{(2\pi)^2} \frac{1}{L_S(\Phi_{\text{ext}}) + L_g/4}, \quad (2.61)$$

which depends on the geometric inductance of the DC-SQUID loop as the JJs with the Josephson inductance,  $L_J(\Phi_{\text{ext}})$  are connected in series to a loop segment each with an inductance  $L_g/2$ . The SQUID-inductance,  $L_S(\Phi_{\text{ext}}) = L_J(\Phi_{\text{ext}})/2$  is defined as

$$L_S(\Phi_{\text{ext}}) = \frac{\Phi_0}{4\pi I_{c0} |\cos(\theta(\Phi_{\text{ext}}))|}, \quad (2.62)$$

where  $I_{c0}$  is the unmodulated critical current of the junction and  $\theta(\Phi_{\text{ext}}) = \pi\Phi_{\text{ext}}/\Phi_0$  under the condition that no hysteresis is present.

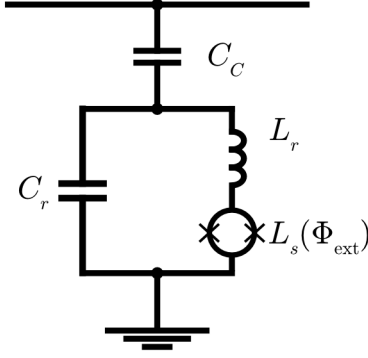


**Figure 2.11:** Schematic of a flux tunable resonator.  $L_S$  is the SQUID-inductance given by  $L_J$  and  $L_g$ .

A Laurent expansion of the left-hand side of Equation (2.60) for  $\omega_c/\omega_0 \approx 1$  gives

$$\frac{\pi\omega_c}{2\omega_0} \tan\left(\frac{\pi\omega_c}{2\omega_0}\right) \approx -\frac{1}{\frac{\omega_c}{\omega_0} - 1} - 1 + \mathcal{O}\left(\frac{\omega_c}{\omega_0} - 1\right). \quad (2.63)$$

Substituting the left-hand side of Equation (2.60) with (2.63), neglecting higher order terms and solving for  $\omega_c$  results

$$\omega_c(\Phi_{\text{ext}}) = \omega_0 \left( \frac{L_r}{L_r + L_S(\Phi_{\text{ext}}) + L_g/4} \right). \quad (2.64)$$

Equation (2.64) describes how the resonance frequency of a flux tunable resonator changes as a function of applied external flux. This dependence is depicted in Figure 2.12. It is observed that  $I_c$  plays a central role in the tuning. Small critical currents would result in a higher Josephson inductance, thus decreasing  $\omega_c$ , and vice versa. Ideally, the current should be low enough that  $\omega_c(\Phi_{\text{ext}} = 0) = \omega_0$  but high enough to significantly tune  $\omega_c$ , see Section 2.4.2.

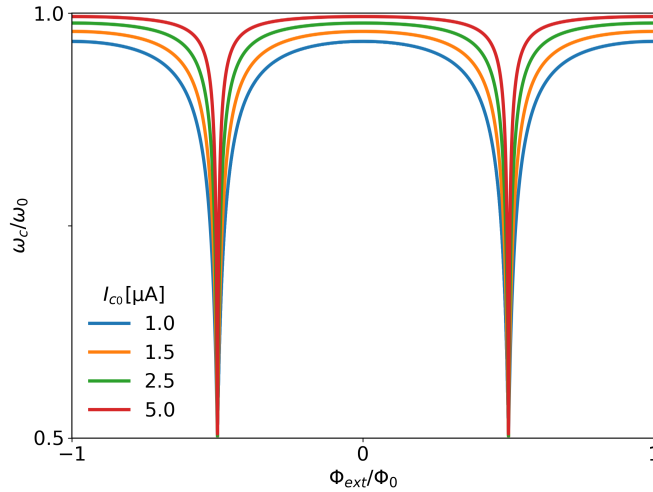


**Figure 2.12:** Frequency modulation as a function of externally applied flux for varying values of critical current of the JJ. For small  $I_{c0}$ ,  $\omega_c$  never reaches  $\omega_0$  due to  $L_J$  being large. On the other hand, large  $I_{c0}$  results in very sharp, but localized modulation of  $\omega_c$  around  $n\phi_0/2$ .

## 2.4 Superconducting levitation

In the following section, requirements to enable magnetic levitation of superconducting particles are described, and inductive coupling between a levitating superconducting particle and a FTR is discussed.

### 2.4.1 Magnetic levitation of a superconducting particle

Levitating superconducting particles using magnetic fields is an approach which enables extreme isolation of mechanical resonators with relatively large masses [24]–[26]. Due to the Meissner-Ochsenfeld effect, superconductors behave as perfect diamagnets, that is, their magnetic susceptibility is  $\chi = -1$ . For a superconductor in a magnetic field  $\mathbf{B}$ , the potential energy is [27]

$$U(\mathbf{r}) = mgz - \frac{1}{2}V\mathbf{M}(\mathbf{r})\mathbf{B}(\mathbf{r}) = mgz - \frac{\chi|B|^2V}{2\mu_0}, \quad (2.65)$$

where  $m$  and  $V$  are the mass and volume of the particle respectively,  $z$  the coordinate in the vertical direction,  $\mu_0$  and  $g$  the magnetic permeability of vacuum and gravitational acceleration respectively. Particles will thus levitate at a point,  $\mathbf{r}_{\text{lev}}$ , where the gravitational and magnetic force on the particle are in balance,  $\mathbf{F}_{\text{total}} = \mathbf{0}$ , such that

$$\mathbf{F}_{\text{total}}(\mathbf{r}_{\text{lev}}) = -\nabla_{\mathbf{r}}U = \frac{\chi V}{\mu_0}\mathbf{B}\nabla_{\mathbf{r}}\mathbf{B} - mg\hat{\mathbf{e}}_z = 0, \quad (2.66)$$

meaning, levitation occurs when  $\mathbf{B}\nabla_{\mathbf{r}}\mathbf{B} = -\rho g\mu_0\hat{\mathbf{e}}_z$ .  $\hat{\mathbf{e}}_z$  is the unit vector in the vertical direction and  $\rho$  is the density of the particle. For levitation to be stable, the local energy minimum at  $\mathbf{r} = \mathbf{r}_{\text{lev}}$  must fulfill

$$\frac{\partial^2 U(\mathbf{r})}{\partial x^2} > 0, \quad \frac{\partial^2 U(\mathbf{r})}{\partial y^2} > 0, \quad \frac{\partial^2 U(\mathbf{r})}{\partial z^2} > 0, \quad (2.67)$$

with  $x$  and  $y$  denoting the horizontal and  $z$  the vertical directions [27]. These conditions imply that the particle will be subject to a restoring force when displaced in any direction.

### 2.4.2 Coupling of a levitating superconducting particle to a flux tunable resonator

Detecting the amplitude of the centre-of-mass motion,  $x_{\text{amp}}$ , of a levitated superconducting particle is essential for cooling it down to the motional ground state [28]. In order to cool the center-of-mass (COM) motion of the particle down to its ground state, the detection has to be sensitive enough to measure amplitudes equal to the zero-point fluctuation of the COM motion of the particle.

Passive cooling with a dilution refrigerator to mK temperatures is not sufficient to reach the ground state, as the effective temperatures of the ground state of motion of the mechanical modes are in the order of nK. Therefore, active cooling is needed to reach the ground state. Active cooling can be done via coupling the COM motion of the particle, directly [29] or indirectly [25], to a FTR. In a direct coupling approach, the magnetic signal of the levitating particle signal modulates the frequency of the FTR directly. In an indirect coupling approach, an intermediate coil is used to transport the signal to the SQUID. The single-photon coupling,  $g_0$ , describes the cavity frequency shift due to the COM motion of the particle when the cavity is populated by a single photon. The particle motion modulates the resonance frequency of the FTR,  $\omega_c$ , according to [29]

$$g_0 = \frac{\partial\omega_c}{\partial x}x_{\text{amp}} = \frac{\partial\omega_c}{\partial\Phi}\frac{\partial\Phi}{\partial x}x_{\text{amp}}, \quad (2.68)$$

where  $\partial\omega_c/\partial\Phi$  is the flux modulation of the FTR resonance frequency,  $\partial\Phi/\partial x$  is the flux captured by the pickup loop per unit of displacement of the levitating particle, and  $x_{\text{amp}}$  is the amplitude of the COM motion of the resonator. For the desired coupling rate,  $\partial\omega/\partial\Phi$  has to be in the order of  $\text{GHz}/\Phi_0$  and the variation of this modulation should be less than 10% [30]. Measuring this  $\partial\omega/\partial\Phi$  is the goal of this thesis.



# 3

## Methodology

The concepts behind the simulations of the CPW resonators are introduced in this chapter, followed by a presentation of the cryostat and experimental setup used in this thesis. Furthermore, the fabrication procedure of the samples, in terms of superconductor deposition, lithography and etching, is described, along the steps that are required to fabricate flux-tunable resonators. Lastly, the experimental procedures that are utilized are also discussed.

### 3.1 Simulation of superconducting resonators

In order to model the propagation of electromagnetic fields in different materials, numerical simulations are performed on ANSYS HFSS. The simulation is done by discretization of the geometry using finite element method (FEM) to solve Maxwell equations. A file of the sample design containing eight superconducting resonators is imported to HFSS ANSYS. In the simulation model, the chip is modelled to be a 2D surface with no thickness, which is placed on top of a 3D box acting as the substrate. A uniform mesh grid is then assigned to the ground layer. The geometrical dimensions of superconducting resonators range from millimeter (length of the CPW resonator), to micrometer (dimensions of the CPW cross-section), for which smaller dimensions require finer mesh elements. As finer mesh grid for the entire sample implies more accurate and detailed simulation, a higher memory usage and more computational power is required. To reduce the necessary memory usage, a 3D mesh box is created around only one resonator that is to be analyzed resonator, together with a portion of the feedline, with a length based mesh constraint  $\leq 20 \mu\text{m}$ , see Figure 3.1a. Half the mesh box lies in the substrate and the other half in the air to simulate the electric field in a 3D space. A lumped element is placed on either side of the feedline, which dictates the direction of the applied signal, to which the impedance is set to be  $Z_0 = 50 \Omega$ . For a FTR, there is an additional lumped-element at the open end of the resonator, to which the inductance and capacitance of the SQUID is assigned.

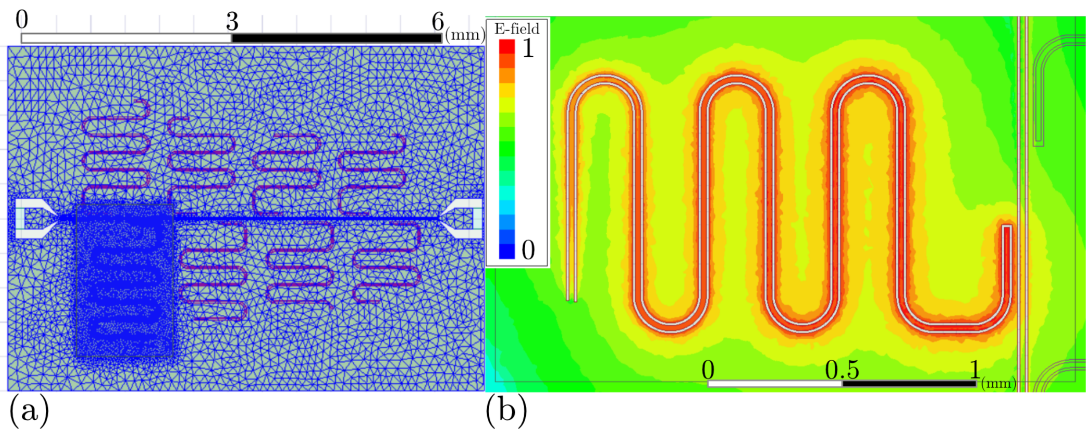


**Figure 3.1:** (a) Simulation of the ground plane. The bounding box is enclosing the resonator and a portion of the feedline. The mesh grid inside the bounding box is much finer compared to the grid in the entire ground plane. (b) Normalized electric field distribution over one resonator. The electric field is normalized to  $4 \times 10^{11}$  V/m. The voltage distribution is concentrated along the meandered resonator and is weakest at the ground-end.

In order to simulate the chip as a superconductor, the ground plane and the resonator are assumed to be a perfect conductor. The Meissner-Ochsenfeld effect and properties, such as  $\lambda_L$  or  $\xi$ , are thus not considered in this simulation. Simulating the chip as a perfect conductor means that conductivity is infinite. As the mesh grid is defined, the Maxwell equations are ready to be solved via FEM. Solving the Maxwell equations yield the electromagnetic field distribution of the feedline and the resonators, as well as across the resonators themselves.  $\omega_0$  and  $Q_C$  of each resonator are also obtained from the simulations.

## 3.2 Cryogenic measurements

Superconducting materials require cryogenic temperatures. Therefore, to measure and characterize superconducting devices, it is essential to cool down to cryogenic temperatures. Cryostats, such as dilution refrigerators, are necessary tools to conduct these experiments. The working principle of a dilution refrigerator is presented in this section alongside the experimental setup used to characterize the resonators, as well as the fabrication and measurement methods.

### 3.2.1 Cryostat

The experimental set-up is inside a BlueFors dilution refrigerator, which has six stages, each hanging from another. The temperature of these stages decreases from room temperature at the very top to mK at the very bottom, see Figure 3.2.

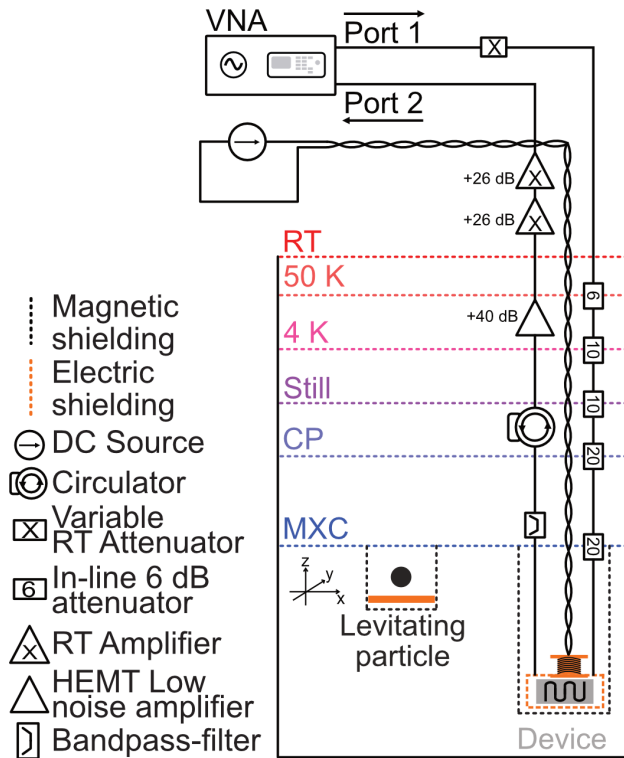


**Figure 3.2:** A schematic representation of the dilution refrigerator and the experimental set-up. The stages are: Room temperature (RT), 50 K, 4 K, Still ( $\sim 800$  mK), Cold plate (CP,  $\sim 100$  mK) and Mixing chamber (MXC,  $\sim 15$  mK). The CPW-devices are mounted inside a sample holder which is electrically shielding the devices, while a can around the sample holder provides the magnetic shielding. Port 1 sends signals to the device and port 2 receives signals returning to the VNA.

The primary cooling method of the refrigerator is adiabatic compression and expansion of  $^4\text{He}$  using a pulse tube cooler [31]. This process can cool the setup from room temperature to roughly 4 K. Cooling below 4 K requires dilution cycle of  $^3\text{He}/^4\text{He}$ -mixture. As the pulse tube cools the

fridge below 4 K, the  $^3\text{He}/^4\text{He}$ -mixture that circulates in the lower plates condenses. Pumping the mixture evaporates  $^3\text{He}$ , as it has higher vapor pressure than  $^4\text{He}$ . This evaporation results in further cooling of the mixture to 800 mK. At this temperature, a phase separation occurs such that the heavy  $^4\text{He}$  settles to the bottom of the mixture container, and lighter  $^3\text{He}$  floats on the top. From this point onwards, mostly  $^3\text{He}$  with trace amounts of  $^4\text{He}$  will circulate in the dilution circuit of the fridge. When  $^3\text{He}$  is pumped back into the liquid mixture, it dilutes inside the  $^4\text{He}$  at the MXC-stage. This dilution is endothermic and absorbs heat from the MXC-stage, cooling it to about 10 mK.

### 3.2.2 Setup

The setup used in the experiments uses two separate electrical lines, see Figure 3.2. One line starts and ends at the VNA, which is used to measure the microwave properties of devices. This line is the microwave (RF) line and is shown as the solid black line labeled as "Port 1" and "Port 2" in Figure 3.2. The other line, the direct current (DC) line, is connected to a coil on top of the sample box, containing the CPW-devices.

Microwave signals are sent from the VNA to the device inside the cryostat. The signal is attenuated by adding room temperature attenuators between the VNA and the cryostat, reducing the input power. Inside the cryostat, further attenuators are found at each stage which attenuate the signal and thermal noise from the respective stages, resulting in a total attenuation of 66 dB inside the refrigerator. The output line from the device to the VNA contains the following elements:

1. A bandpass filter at the MXC-stage. This attenuates any signals outside the 4-8 GHz frequency band.
2. A Circulator at the CP, whose purpose is to block reflected signals that might otherwise propagate back to the sample.
3. A high electron mobility transistor (HEMT) at the 4 K stage. The HEMT is a low-noise amplifier that amplifies the signal by 40 dB.
4. Two room-temperature amplifiers outside the fridge. Each amplifier amplifies the signal by 26 dB.

The sample is inside a niobium can, covered with cryoperm tape and aluminum tape. Cryoperm, a Fe-Ni alloy, functions as a ferromagnetic shield, whereas both aluminum and niobium are superconductors, providing further magnetic shielding. The sample itself is contained in a sample holder made from Cu, which is inside the magnetic shield (see Figure 3.3). The sample is glued inside and grounded to the sample holder via Al wirebonds. The sample holder is electrically grounded and provides a vacuum beneath and above the sample to avoid parasitic capacitance. The sample holder fully encloses the sample, protecting it from electromagnetic radiation by absorbing incoming photons, that are transformed into heat in the sample holder. The heat is transferred to the sample stage and away from the sample, thereby isolating from electromagnetic waves.

The sample is wirebonded to an SMA connector pin, which is in turn connected to the VNA via the RF line. The purpose of the DC line is to supply a current to the coil, used to flux bias the SQUIDS of the flux-tunable resonators, see Section 2.3.

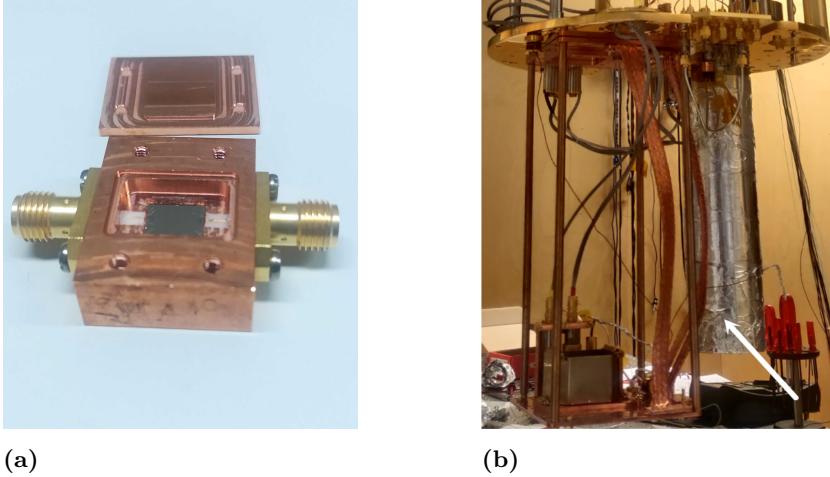


**Figure 3.3:** (a) The sample holder for the CPW and FTR devices. SMA connectors are attached to both sides of the box. (b) Magnetic shield can. The arrow points to where the sample holder lies within the can.

### 3.3 Device fabrication

The fabrication of the critical current density bridges, the linear CPW resonators and the FTR start with metal deposition and patterning of the ground plane. An additional step is the fabrication of JJs which is unique for FTRs. The fabrication procedure for the bridges and CPWs are as follows:

1. Cleaning of 2-inch wafer substrate. The wafer is submerged in HF to strip the oxide layers off the substrate.
2. Deposition of superconducting thin-film ground plane
3. Lithography and etching
- \*4. Shadow Evaporation
- \*5. Lithography and etching of contact pads
6. Dicing the wafer into separate  $7 \times 5$  mm chips

Steps 2 and 3 will be discussed more in detail in Section 3.3.1. Steps \*4 and \*5 are part of the fabrication process of the FTRs, which will be discussed in Section 3.3.2. The fabrication is done in the Nanofabrication Laboratory at MC2, Chalmers.

#### 3.3.1 Fabrication of critical current density bridge and CPW

Thin-film superconducting devices are fabricated by deposition of superconducting metals and patterned via lithography and etching. This section covers deposition via sputtering and the metal layer patterning via lithography and etching.

##### 3.3.1.1 Superconductor deposition

Al or Nb are deposited by sputtering. In sputtering, atoms are ejected from a source metal when they are bombarded with ionized gases, such as Ar, onto a 2-inch Si-wafer. Al is a commonly used type-I superconductor for fabrication of superconducting circuits, due to  $T_c$  being higher than the temperatures of commercial dilution refrigerators. Nb is also of interest as  $T_c$  and  $H_c$  are higher than those of Al, potentially allowing for direct coupling to the levitating particle in a high magnetic field due to its tolerance to higher magnetic fields than Al. 300 nm Al or Nb are deposited for the bridges used for characterizing the critical current density,  $j_c$ . 150 nm Al or Nb are deposited for the bare superconducting CPW.

##### 3.3.1.2 Lithography and etching

A positive photoresist layer is spin-coated on the metal thin-films. The exposure of the patterns is done via a laser writer. After developing the exposed resist, residual photoresist is ashed using

oxygen plasma. Al is wet-etched by submerging the wafer in an Al etchant bath. Nb is etched with Cl ions via reactive ion etching.

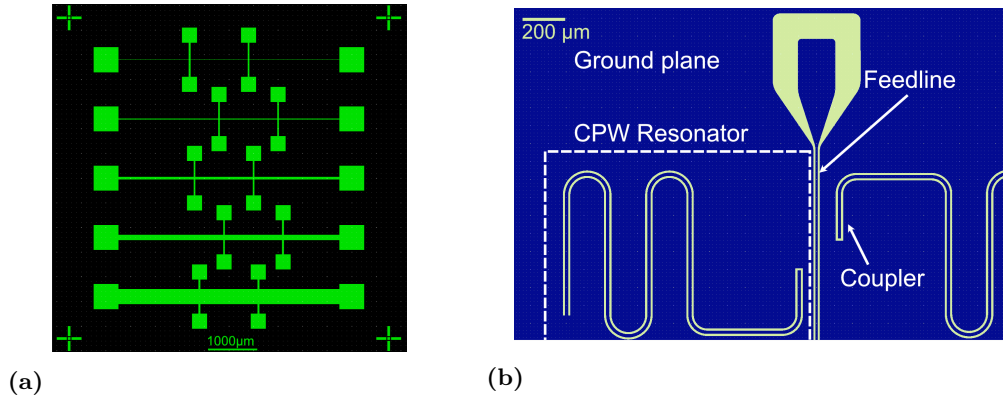


**Figure 3.4:** (a) Bridges of different widths. (b) A  $\lambda/4$  CPW coupled to the feedline.

### 3.3.2 Fabrication of flux-tunable resonators

The ground plane and the CPW resonators and feedline are fabricated via physical vapor deposition (PVD) and etching as described above. In PVD, metal atoms are evaporated via electron beam from a source metal, and condensed on the target. Shadow evaporation and the contact pad lithography is described in this section.

#### 3.3.2.1 Shadow evaporation

The JJs are fabricated at the gap terminating the CPW resonators at the ends away from the feedline, via shadow evaporation [32]. The shadow evaporation process allows for control of the oxide layer thickness of the junctions in vacuum, in a single deposition step via PVD. The wafer is spin-coated twice, initially with a thicker, followed by a thinner photoresist. The thicker photoresist is overexposed such that an undercut is formed. The thinner resist then functions as a cover for when the junction is deposited. First, the JJs are patterned via electron-beam lithography (EBL). Next, the wafer is placed under high-vacuum where the source metal, Al, is aligned perpendicular to the device. By tilting the device at a certain angle, the first junction electrode is deposited. The electrode is then subject to a high precision oxidation, designed to form an insulating oxide layer of thickness 1 nm. The device is then aligned back to its planar state, rotated and again tilted to deposit the second junction electrode, see Figure 3.5.

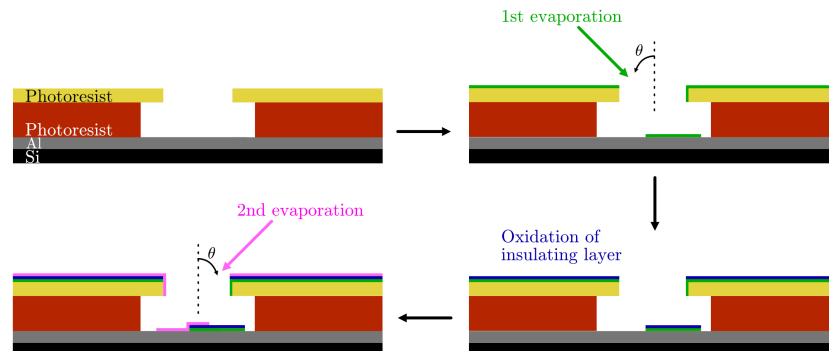


**Figure 3.5:** Schematic overview illustrating shadow evaporation.

#### 3.3.2.2 Lithography and etching of contact pads

Two contact pads are then patterned, again via EBL, where 150 nm Al is deposited, via PVD, on top of the electrodes, see Figure 3.6. Both resists are then removed by lift-off.

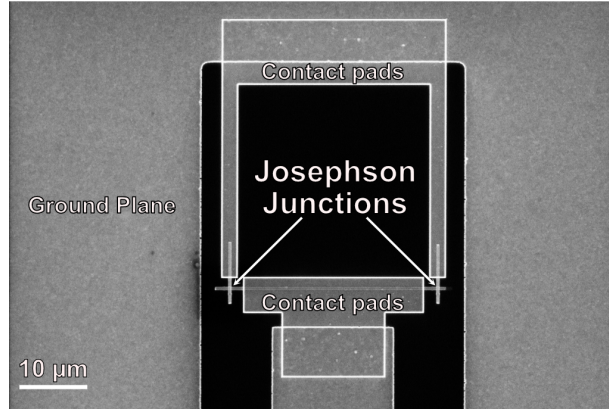


**Figure 3.6:** A fabricated SQUID-cavity connected to the central conductor of the CPW. The junction electrodes are 400 nm in width and the loop size is  $30 \times 30 \mu\text{m}^2$ .

## 3.4 Measurement Setup

### 3.4.1 Determination of critical current density

In order to determine  $j_c$ , the bridges are glued on top of a sample holder, which, via wirebonds, are connected to the DC-line (see Figure 3.2). Current is then supplied to the bridge using the DC current source via the DC-line. A RuOx temperature sensor is attached next to the sample holder to monitor change in temperature, see schematic in Figure 3.7. The current is continuously increased until  $I_c$  is reached, thereby destroying superconductivity, which will result in a sharp increase in temperature at the MXC-stage. Dividing the measured  $I_c$  by the cross-section results in  $j_c$ . Measuring  $j_c$  of thin-film superconductors is necessary in order to determine the maximum power that can be tolerated before becoming normal conducting.

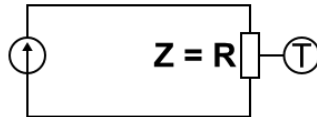


**Figure 3.7:** Schematic of the experimental setup to determine  $j_c$ . A DC source supplies current to the samples, which are near a RuOx-temperature sensor.

### 3.4.2 Resonator characterization

Superconducting resonators, both linear and flux-tunable, are characterized by measuring the transmission scattering parameter to determine properties such as  $\omega_0$  and quality factors. The frequency modulation of flux-tunable resonators is also studied, as this is one of the factors that determines the coupling rate between the levitating superconducting particle and the FTR frequency.

#### 3.4.2.1 Resonance frequency and quality factor

The goal of characterizing the superconducting resonators is to identify  $\omega_0$  for each resonator and compare to them with the designed frequencies. This is done by scanning over a wide frequency span of 4-8 GHz from the VNA at relatively high powers and identifying sharp drops in the microwave transmission spectrum, see Figure 3.8.

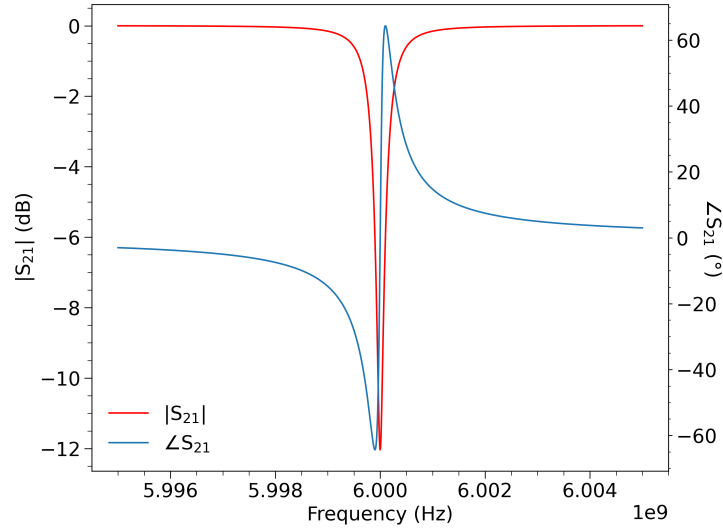


**Figure 3.8:** The scattering parameters of an ideal resonator described in Section 2.2.5

The aim of these measurements is to determine the power dependence of  $\omega_0$  and quality factors in terms of the number of intra-cavity photons. The quality factors of both linear and flux-tunable CPW resonators are important because they will determine the sensitivity with which the particle motion can be detected. The input power is continuously decreased while the transmission scattering parameter data is recorded, which is then processed with the fitting procedure described in Section 2.2.5 from which  $Q_i$ ,  $Q_c$  and  $\omega_0$  can be calculated. The intra-cavity photon number is found by using Equation (2.59), so that the change of quality factors as a function of photon number can be determined. The experimental setup is depicted in Figure 3.9

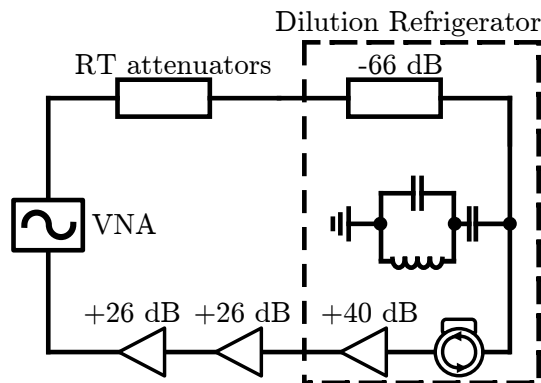


**Figure 3.9:** Schematic of the setup for measuring microwave transmission spectrum. The measured samples and microwave components are inside the dilution refrigerator.

### 3.4.2.2 Flux tunability

The first task is to identify  $\omega_0$  of the flux-tunable resonators (FTR) with no modulation. This is done in the same way as described in section 3.4.2.1. In order to characterize the flux tunability, an electric current is applied to the coil resting on top of the FTR. Figure 3.10 shows the schematic of the experimental setup. By increasing the applied current,  $\omega_0$  of the FTRs will change as illustrated in Figure 2.12, with which the current bias corresponding to the interval  $-1/2 \leq \Phi_{\text{ext}}/\Phi_0 \leq 1/2$  is found. By expressing  $\omega_0$  as a function of  $\Phi_{\text{ext}}$  and simply taking the derivative, we can calculate  $\partial\omega_0/\partial\Phi_{\text{ext}}$ , which is one of the factors that is needed to determine the particle-to-FTR coupling rate.

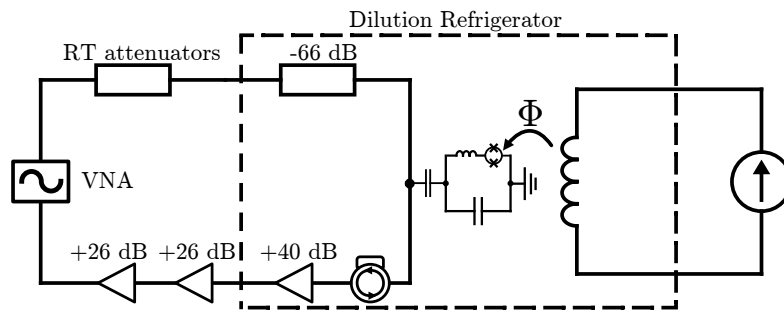


**Figure 3.10:** Schematic of the setup for identifying the flux tunability.

# 4

## Results

This chapter is briefly introduced with the results of the measurement for  $j_c$  of the Al superconducting bridges, followed by a comparison to previously reported values. This introduction is followed by the results of the linear CPW resonator characterization in Section 4.2, which constitute half of the chapter. The calculated and measured values of Al and Nb resonators are presented, with comparison to the state of the art for each material. Analytic results as well as experiments and characterization of Al FTR are shown in the latter half of the chapter.

### 4.1 Superconducting properties of Al

The temperature at the sample stage was measured via a RuOx-sensor, as a function of applied current on the Al sample. A sharp temperature increase can be observed at  $I \approx 10\text{mA}$  for the bridge width of  $300\ \mu\text{m}$ , see Figure 4.1. As the sputtered thickness is  $300\ \text{nm}$ ,  $j_c$  is determined to be approximately  $1.11 \times 10^8\ \text{A/m}^2$ . The determined  $j_c$  is smaller by 2 to 3 orders of magnitude than previously measured values for structures with similar cross-sections, that were evaporated rather than sputtered [33]–[35]. The difference in deposition could be a possible explanation for the lower  $j_c$  value.

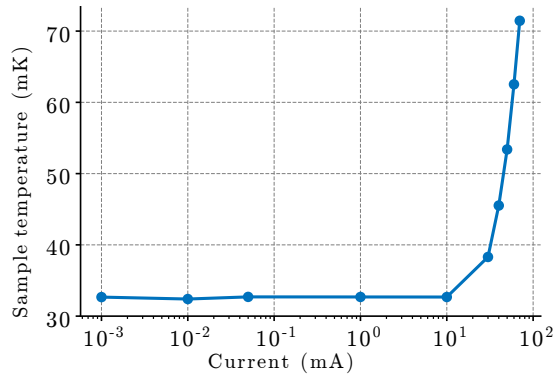


**Figure 4.1:** Sample temperature as a function of applied current for a bridge with cross-section of  $300 \times 0.3\ \mu\text{m}^2$ . An abrupt increase in temperature is observed around 10 mA.

### 4.2 CPW Resonator characterization

In the case of Al, the CPW resonators were measured at a range of 20 to -25 dBm output power from the VNA with no attenuation, shown in Figure 4.2a. At low powers, the  $S_{21}$  response at resonance is symmetric. However, as the power increases, the electromagnetic fields increase as well, decreasing the density of Cooper pairs and thus, increasing the kinetic inductance [36]. Thereby the resonance frequency shifts to lower frequencies, see Equation (2.42), as shown for the range of -25 to -5 dBm in the power sweep. At even larger powers, superconductivity breaks, causing the kinetic inductance to suddenly vanish, shifting the resonance frequency up (0 to 20 dBm). At that point, the peak shows a positive non-linearity, meaning that the dip is asymmetric and is skewed towards higher frequencies. As the VNA cannot interpret multivalued results, this expresses as an abrupt increase in the transmission response.

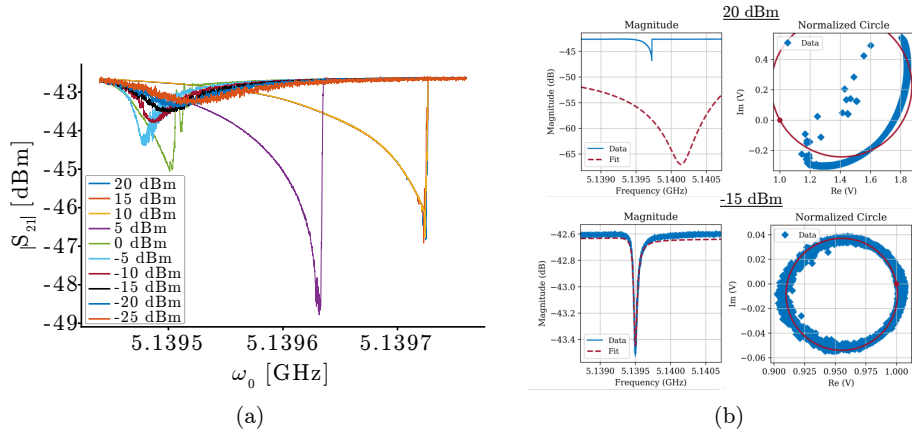


**Figure 4.2:** (a) Power sweep of an Al CPW resonator at  $\omega_0 \approx 2\pi \times 5.15$  GHz from 20 dBm to -25 dBm VNA output power.  $\omega_0$  shifts for varying powers. Superconductivity is broken at high powers. (b) Unsuccessful and successful model fits of measurement data for 20 and -15 dBm, respectively.

The data fits for  $\omega_0 \approx 2\pi \times 5.15$  GHz between 20 dBm and -15 dBm, respectively, are shown in Figure 4.2b. It is observed that the model, the red dashed line, is unsuccessful and does not fit the measured resonance dip for 20 dBm. However, for symmetric resonance dips, as for the -15 dBm case, the fit matches the measurement data as intended.

Measurement experiments for Al and Nb CPW resonators were performed as described in Section 3.4.2, using the experimental setup presented in 3.2.2, however, without any room temperature amplifiers. Each sample was designed with eight resonators. Figure 4.3 shows the  $S_{21}$  transmission data of the Al and Nb samples. The obtained signal contains the transmission of the entire system, that is from the VNA to the samples, where on that signal the signatures of the resonators are observed as dips. The measurements for the Al samples had a VNA output power of 0 dBm which was attenuated with 35 dB room temperature attenuators, whereas the Nb measurements were done with an output power of 20 dBm and 60 dB room temperature attenuation. The arrows indicate the frequencies in which the resonances of the CPW resonators were determined. All eight resonance dips of the CPW resonators on the Al chip were found in the measurement. However, the arrow with a star indicates a frequency response in which none of the resonators were designed for. The origin of this response was not further investigated. Seven out of the eight resonance frequencies were measured for the Nb sample. The broad resonance around 7.1 GHz is attributed to the feedline. This is due to impedance mismatch between the feedline and wirebonds that connect the samples to the RF lines. This in turn "buries" the resonance dip of that resonator within that frequency range.

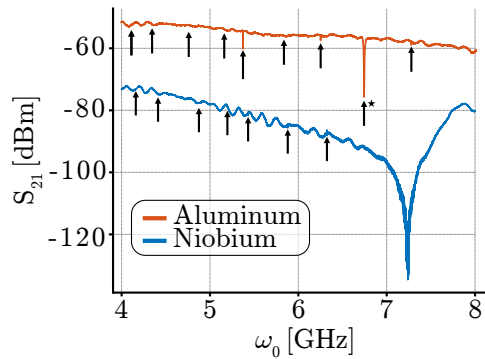


**Figure 4.3:** 4 to 8 GHz measurement of the Al and Nb resonators. The black arrows mark the resonance frequencies of the CPW resonators. The arrow with a star is not a resonance frequency of any Al CPW resonators.

The analytic, simulated and experimental values of  $\omega_0$  and  $Q_C$ , as well as the experimental values for  $Q_i$ , for the Al and Nb CPW resonators, as a function of the inverse resonator length, are shown in Figure 4.4. The analytic values for  $\omega_0$  and  $Q_C$  are calculated via Equations (2.42) and (2.39) respectively. The simulated values for  $\omega_0$  and  $Q_C$  are extracted from ANSYS HFSS simulations described in Section 3.1. The experimental values for  $\omega_0$ ,  $Q_C$  and  $Q_i$  are obtained via the fitting procedure described in Section 2.2.5.

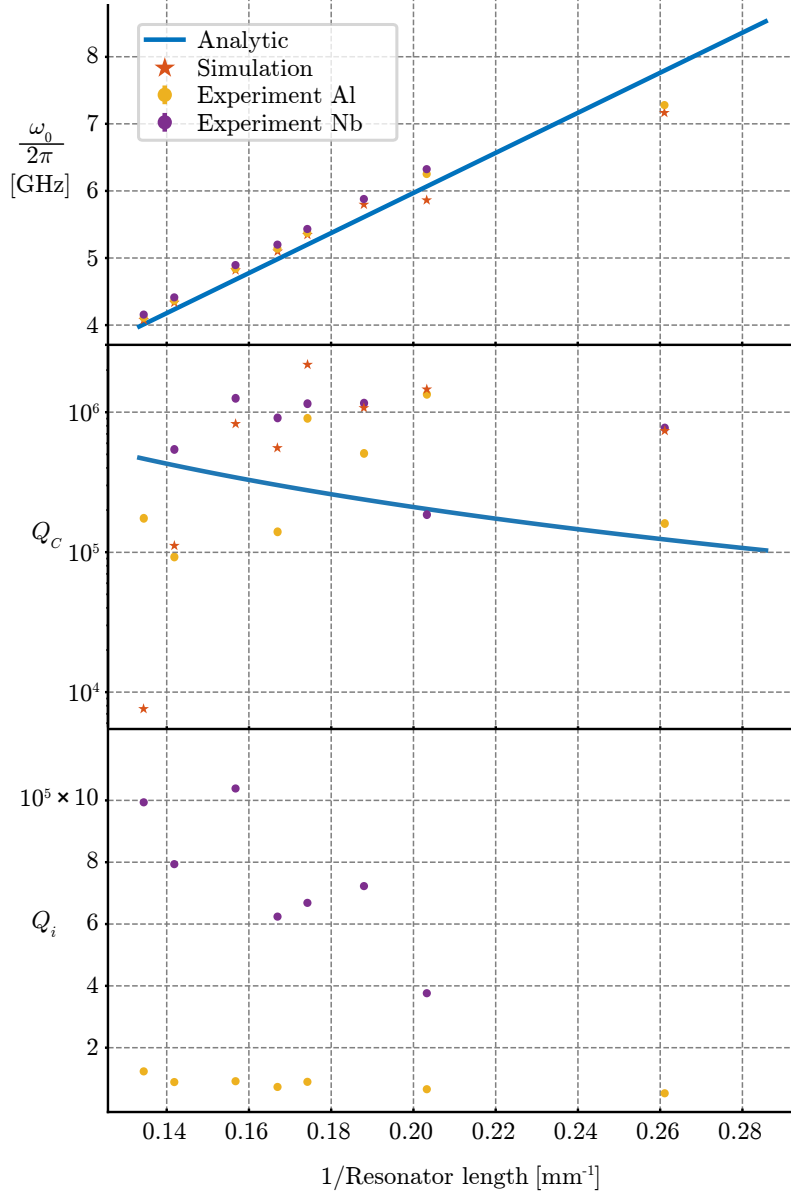


**Figure 4.4:** Analytic, simulated and measured resonance frequencies ( $\omega_0$ ), coupling ( $Q_C$ ) and measured internal ( $Q_i$ ) quality factors for CPW resonators of different lengths and materials, as a function of inverse resonator length. The experimental values correspond to  $10^8$  and  $10^6$  average number of intra-cavity photons for Al and Nb, respectively. The values obtained from simulations are independent of the superconducting material, as opposed to the analytic and experimental values.

It is observed that  $\omega_0$  is proportional to inverse resonator length, for the analysis, simulation as well as the experiments. This is due to the inductance and capacitance being bound to the geometry, mainly the length, of the resonators. The experimental and simulated frequencies match well with the analytic evaluation.

Analytically,  $Q_C$  decreases slightly for higher values of  $\omega_0$ , according to Equation (2.40). Simulations and experimental results, however, do not show any clear dependence on frequency.

Decreasing the error tolerance in the simulation, could potentially yield in more accurate results, however no clear conclusion can be drawn from the simulated or experimental values.

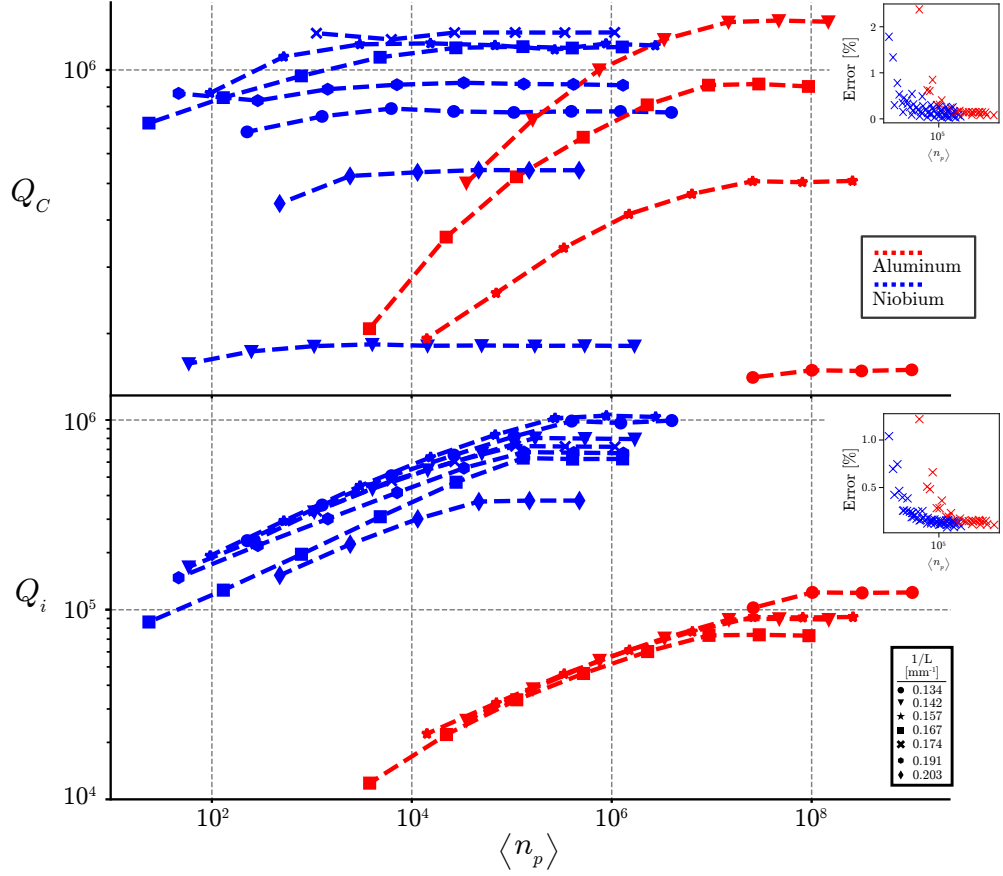
Only experimental results are presented for the internal quality factor,  $Q_i$ , as they cannot be easily calculated. It is observed that Nb CPW resonators have larger  $Q_i$  compared to Al, where previously reported values indicate that  $Q_i$  for Al is larger than Nb, see Figure 4.6.  $Q_i$  for both Nb and Al decreases for higher  $\omega_0$ . However, the change in  $Q_i$  is more pronounced in Nb compared to Al, which remains fairly constant at approximately  $1 \times 10^5$ .

The upper graph in Figure 4.5 shows  $Q_C$  as a function of the average intra-cavity photon number, for Al and Nb. For Nb,  $Q_C$  shows a weak dependence on  $\langle n_{ph} \rangle$ , where a decrease in  $Q_C$  can be observed at lower powers. Al resonators, show similar results, however the decrease is more pronounced.:  $Q_C$  decreases with decreasing number of circulating photons. This result is unexpected, seeing as  $Q_C$  is bound to the design of the resonators and should remain constant, regardless of power. The source of the decrease for both Al and Nb stems from insufficient mathematical fitting, where the entire measurement data was not fitted perfectly, yielding in the observed decrease. The fitting can be improved through increasing measurement parameters in the VNA, such as adjusting the IF bandwidth and thereby improving the signal-to-noise ratio.

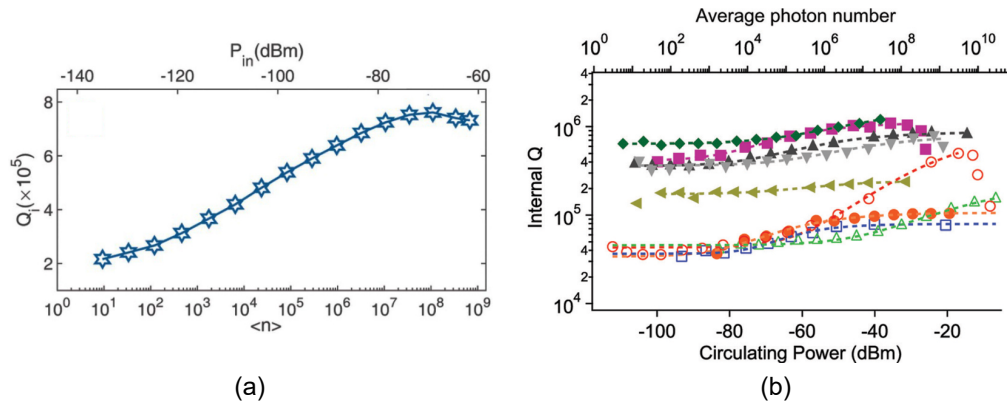
The lower graph in Figure 4.5 shows  $Q_i$  for Al and Nb as a function of the average intra-cavity photon number. It is expected that the measurements should reach powers corresponding to  $\langle n_p \rangle \approx 1$ , see Figure 4.6. The measurements for Al and Nb, however, do not reach this low power, as room temperature amplifiers were not available at the time of the experiments for neither Al nor Nb. The RT amplifiers would amplify the signals returning from the samples to the VNA and would increase the signal-to-noise ratio.  $Q_i$  is higher for Nb than Al. A similar trend is observed for both materials: At the regime where a high number of photons is circulating inside the resonator,  $Q_i$  is constant and decreases for lower number of photons. The decrease in  $Q_i$  can be explained in terms of loss mechanisms: Material defects present in the native oxide present at the interface between the substrate and superconductor, or the interface between superconductor and vacuum, create two-level systems (TLS), which interact with the resonator and absorb photons from it. As the power circulating in the resonator is increased, TLS begins to saturate and so the fraction of energy lost from the resonator decreases, in other words,  $Q_i$  increases [37]. At larger powers, the TLS are all fully saturated and the  $Q_i$  value reaches its maximum and stays constant. As  $\langle n_p \rangle$  decreases, the TLS competes with the resonator to absorb photons, and losses from TLS become more dominant, lowering  $Q_i$ . It is expected that, at lower photon numbers, the decrease will halt and  $Q_i$  will become constant again as the thermal fluctuations from the environment dominate compared to the power from the photons inside the resonator.

Figure 4.6a shows measured  $Q_i$  for superconducting Al CPW resonators evaporated on sapphire [38]. For high power, where TLS-losses are saturated,  $Q_i \approx 8 \times 10^5$  where it decreases to  $Q_i \approx 2 \times 10^5$  at around  $\langle n_p \rangle = 10$ . The previously reported values are ten times larger than the measured Al CPW resonators in this work. This is attributed to the difference in deposition, where sputtering introduces more defects in the interface between substrate and superconductor, such as parasitic TLS, compared to evaporation. Furthermore, by cleaning samples with hydrofluoric acid (HF) strips native oxide layers from the substrate [39], or through ultrasonication [38], would also increase  $Q_i$ . Furthermore, depositing on sapphire would also result in a larger  $Q_i$ .

$Q_i$  for the measured Nb CPW resonators is twice higher than previously reported values, as shown in Figure 4.6b [40]. The highest reported  $Q_i$  is for 200 nm thick Nb thin-film sputtered onto 500  $\mu\text{m}$  Si/SiO<sub>2</sub> substrate, where  $Q_i \approx 7 \times 10^4$  for  $\langle n_p \rangle = 10^6$ . This is smaller by an order of magnitude compared to the  $Q_i$  at equal  $\langle n_p \rangle$  for the measured Nb CPW in this work.



**Figure 4.5:** Quality factors of Al and Nb resonators from 4 to 8 GHz as a function of intra-cavity photon number. (upper) The coupling quality factor is roughly constant for Nb, but decreases for lower powers for Al. (lower) The internal quality factor showing the losses. Both Al and Nb show similar trends.



**Figure 4.6:** (a)  $Q_i$  as a function of circulating power and equivalent average number of intra-cavity photon numbers for superconducting Al CPW resonators on sapphire [38]. (b)  $Q_i$  as a function of circulating power, with the equivalent average intra-cavity photon number, for superconducting Nb CPW resonators (hollow blue squares) deposited on top of a Si-substrate. [40].

### 4.3 FTR characterization and flux tunability

The analytic calculation of the frequency modulation can be seen in Figure 4.7. For  $\omega_0 \approx 2\pi \times 7.25$  GHz, it can be observed that  $\partial\omega_0/\partial\Phi \approx 2\pi \times 3.64$  GHz/ $\Phi_0$  at  $0.8 \times \Phi_0$ , marked by the tangent line. The dimensions assumed for this FTR were: width of  $800 \times 800$  nm for the JJs, a SQUID-loop area of  $10 \times 10 \mu\text{m}^2$ , where  $I_{c0} = 704$  nA, corresponding to  $L_S = 1438$  pH.

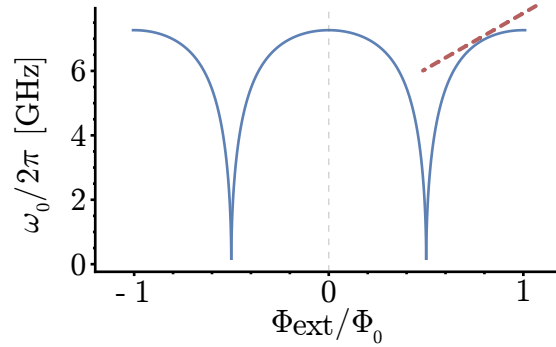


**Figure 4.7:** Analytic determination of the frequency modulation of the FTR for an external flux in the interval of  $[-\Phi_0, \Phi_0]$ . The frequency modulation,  $\partial\omega_0/\partial\Phi$  is marked as the dotted red tangent line at  $0.8 \times \Phi_0$

The FTR experiments were conducted in the same setup as the bare CPW resonators. The flux tunability experiment is described in Section 3.4.2.2. The samples were designed with eight resonators, wherein half of the resonators were linear and the other 4 were flux-tunable. Figure 4.8 shows  $S_{21}$  transmission data of the resonators as a function of frequency at 20 dBm power from the VNA, with an attenuation of 60 dB. Four resonances were identified as linear resonators, indicated with black arrows, and only one FTR was found, indicated with the diamond marked arrow, where  $\omega_0 \approx 2\pi \times 6.29$  GHz.

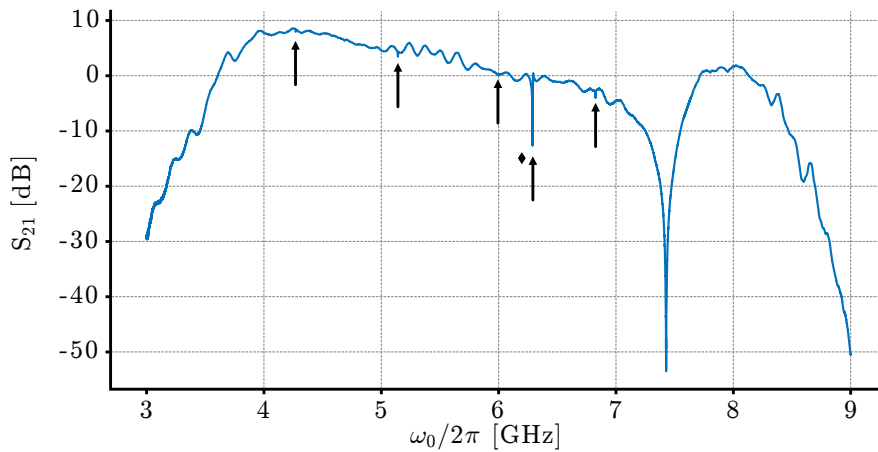


**Figure 4.8:**  $S_{21}$  transmission data of the FTR device made out of Al, as a function of frequency, measured at -106 dBm total power. Five resonance frequencies were detected, indicated by the arrows, out of which one is flux tunable, marked with the arrow with a diamond. The response at 7.4 GHz is the feedline frequency.

The flux tunability of the FTR is shown in Figure 4.9. The  $S_{21}$  transmission data as a function of frequency was recorded for bias currents from -500 to 500  $\mu\text{A}$  applied to the flux-modulation coil. A tunability in the resonance frequency of the FTR is observed, however, it is very weak and does not modulate  $\omega_0$  more than by  $\sim 2$  MHz.

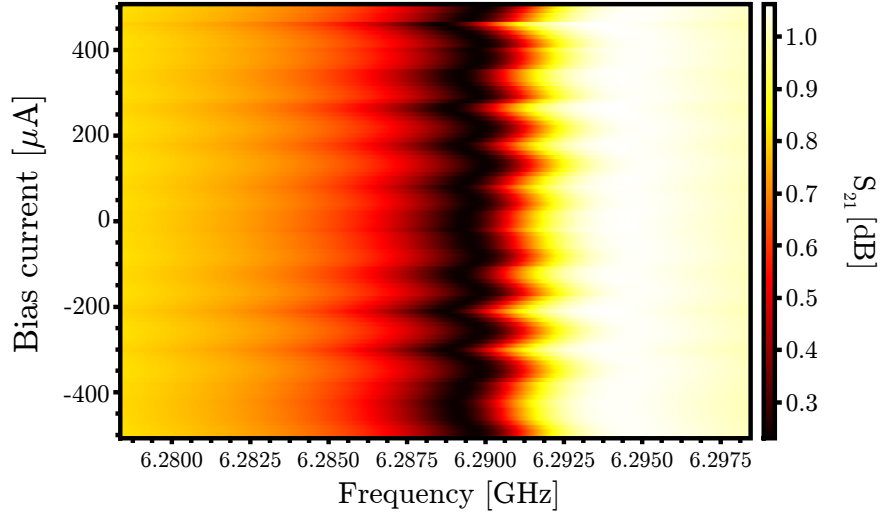


**Figure 4.9:**  $S_{21}$  transmission as a function of frequency and biasing current. The resonance frequency is tuned at approximately  $\omega_0 = 6.29 \times 2\pi$  GHz.

An additional experiment was conducted based on the flux tunability observed in Figure 4.9, where the tuning of  $\omega_0 = 2\pi \times 6.29$  GHz at varying powers over one flux quantum is depicted in Figure 4.9. The inset shows the current range from -165 to -345  $\mu\text{A}$ , where one  $\Phi_0$  corresponds to 105  $\mu\text{A}$  as shown in the graph. The frequency modulation is shown to be at most 1.2 MHz, where  $\omega_0 = 2\pi \times 6.2898$  GHz. There is no sign of any dependence on applied power.

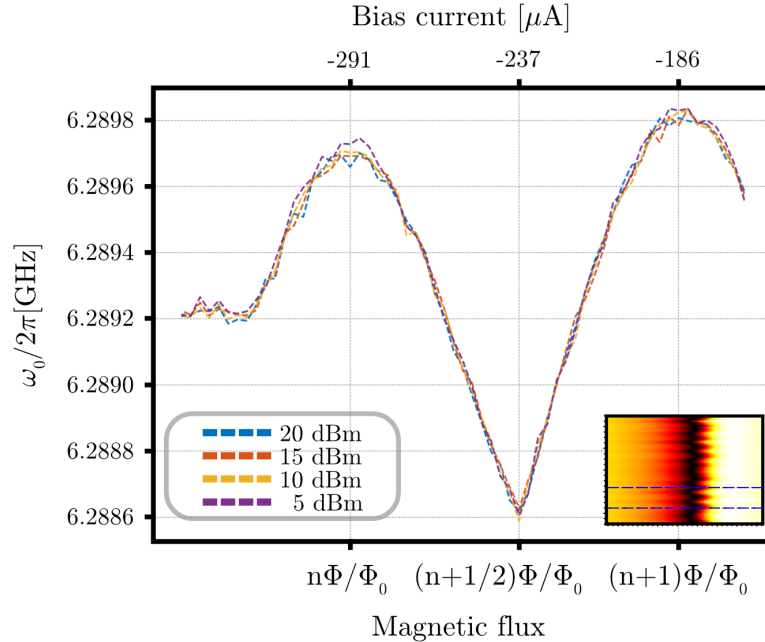


**Figure 4.10:** Frequency modulation of  $\omega_0 = 2\pi \times 6.29$  GHz over one  $\Phi_0$ , at varying power. The respective biasing current applied is also shown. The inset shows the corresponding portion of the  $S_{21}$  transmission data in Figure 4.9.

The weak frequency modulation attributed to the misformation of the fabricated JJs at both sides of the SQUID, see Figure 4.11.

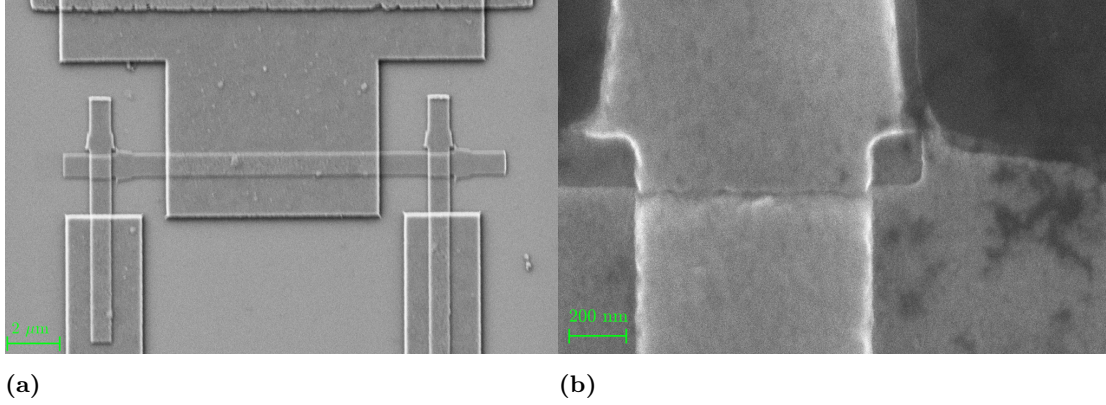


**Figure 4.11:** (a) SEM image of the SQUID-loop. (b) SEM image of the JJs. The deposited edges of the junctions are connected.

The projected features formed due to over-etching of the thicker resist layer. The over-etching causes an undercut where the metal gets deposited, forming the features as shown in Figure 4.11b. This increases the width of both the junctions in that region, enough to create an electric short. These features will thus carry a portion of the current applied to the loop and bypass the junctions, while a portion of the current still runs through the junction as intended. The current bypassing the junctions,  $I_{\text{short}}$ , will be much larger than  $I_c$  across the junctions. A modified form of SQUID inductance (Equation (2.62)), which accounts for  $I_{\text{short}}$ , illustrates the frequency modulation of such a shorted SQUID:

$$L_S(\Phi_{\text{ext}}) = \frac{\Phi_0}{4\pi I_c |\cos(\theta(\Phi_{\text{ext}}))| - \frac{1}{2} \frac{I_{\text{short}}^2}{I_c |\cos(\theta(\Phi_{\text{ext}}))|}}.$$

Additional experiments were attempted with samples with larger loop-areas ( $20 \times 20 \mu\text{m}^2$  and  $30 \times 30 \mu\text{m}^2$ ) and smaller junction widths (600 and 400 nm), however none of the resonance frequencies of the FTRs were detected in the measurements. This is because of longer oxidation times in the shadow evaporation step, where the oxide layer of the junctions should be 3 to 4 nm. A thicker oxide layer decreases  $I_c$ , which will decrease  $\omega_0$ , as per Equations (2.62) and (2.64). The larger oxide layer was found to decrease  $\omega_0$  of the FTRs by a factor of  $\sim 2$ , which resulted in the resonance frequencies to be in the 2-4 GHz range, which is beyond the measurement range of the setup as both the HEMT and bandpass filter amplifies and allows, respectively, signals that are in the 4 to 8 GHz range.

# 5

## Conclusions

In this last chapter, the results of the thesis is summarized along the conclusions that can be drawn. The conclusions lay the ground work for proposed future work, presented in Section 5.2.

### 5.1 Summary

In the thesis work I have successfully fabricated superconducting strips made of Al, where  $j_c$  was determined to be  $1.11 \times 10^8$  A/m<sup>2</sup>, by measuring the temperature as a function of applied current of a bridge with the dimensions  $300 \times 0.3$   $\mu\text{m}^2$ , which is lower than for literature values.

Furthermore, I have fabricated Al and Nb resonators and characterized their microwave properties. I managed to successfully identify the resonance frequencies of seven out of eight resonators, for both the superconducting materials. The measured data was subsequently treated through an fitting algorithm to evaluate the quality factors.  $Q_C$  for both Al and Nb CPW resonator is in the order of  $10^5$ , in which the Nb ones are constant regardless of the number of photons circulating in the resonator as opposed to Al, which shows a decrease of circa 10%.  $Q_i$  for both metals decreases by about 10% for a decreasing number of photons. Nb shows  $Q_i = 10^6$  at high powers, compared to Al for which  $Q_i = 10^5$ , which are close to the  $Q_i$  of the literature.

Lastly, I characterized the flux tunability of an Al sample, containing four flux-tunable and four linear CPW resonators. From the measurements, five resonance frequencies were detected, out of which only one belonged to a FTR. The applied magnetic flux, albeit showing clear signs of frequency tunability, only decreased the resonance frequency by 1.2 MHz for one half  $\Phi_0$ . This frequency tunability is very small, as literature indicates a modulation in the orders of GHz. It is suspected that the difference in frequency modulation comes from the current in the SQUID not passing through the JJs. This additional leakage current resulted from a small bridge at the JJ, which formed during a non-perfect fabrication step.

The measured values for  $\omega_0$  and  $Q_C$  of the CPW resonators are in good agreement with the analytic calculations and simulations of the CPW. This implies that the analytic models and simulation give good estimates for the design of FTRs given the same underlying assumptions as for the linear CPW resonators.

The flux tunability is one of the parameters required to determine the single-photon coupling rate,  $g_0$ , between the FTR and a levitating superconducting particle. However, the unexpectedly low frequency modulation found in the experiment is far from sufficient. The size of the JJs must therefore be reduced in order to ensure that no short is present between the junctions.

### 5.2 Future work

For future work, the first step is to fabricate functional FTRs, which show a frequency tuning in orders of GHz. The fabrication has multiple areas of improvement, such as evaporating the entire ground plane in order to increase the quality factors, as opposed to sputtering it as done for the FTR used in this work [41]. Additionally, using different substrates, for example sapphire, or cleaning the samples with HF would also improve the quality factor [39]–[41].

The magnetic trap which traps the superconducting levitated particle can generate magnetic field with strengths in the order of 10 mT, which higher than  $H_C$  for Al, thus, breaking superconductivity [42]. As  $T_c$  and  $H_c$  for Nb are larger than Al [43], promising possibilities are found in terms of direct coupling a FTR fabricated out of Nb, to the levitating particle. Figure 5.1 shows a proposed schematic set-up for such a direct coupling experiment. The quadrupole

magnetic field traps the particle, for which the modulated magnetic field caused by the particle motion is fed directly to the FTR.

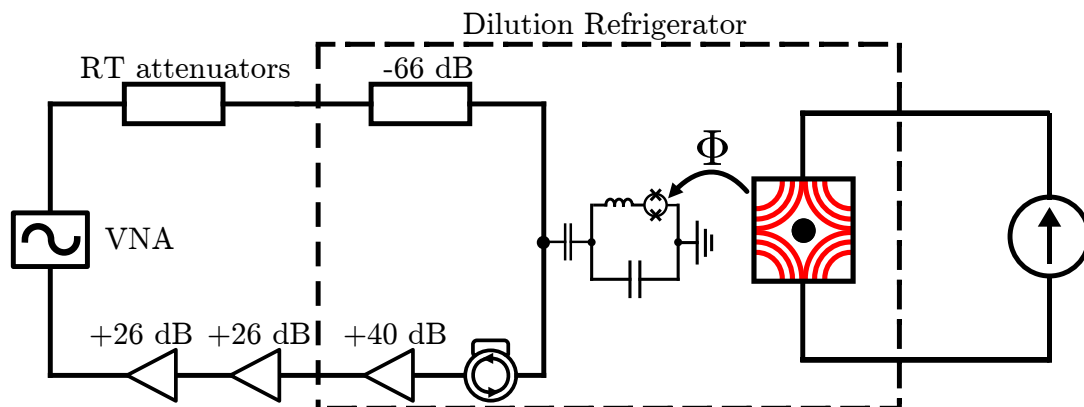


**Figure 5.1:** A proposed experimental setup for the direct coupling experiment. The levitating superconducting particle is trapped inside a quadrupole magnetic field. The field that is modulated by the particle motion is directly fed to the FTR.

# Bibliography

- [1] M. Arndt and K. Hornberger, “Testing the limits of quantum mechanical superpositions,” *Nature Physics*, vol. 10, no. 4, pp. 271–277, Apr. 2014. DOI: [10.1038/nphys2863](https://doi.org/10.1038/nphys2863). [Online]. Available: <https://doi.org/10.1038/nphys2863>.
- [2] M. Arndt, O. Nairz, J. Vos-Andreae, C. Keller, G. van der Zouw, and A. Zeilinger, “Wave–particle duality of c60 molecules,” *Nature*, vol. 401, no. 6754, pp. 680–682, Oct. 1999. DOI: [10.1038/44348](https://doi.org/10.1038/44348). [Online]. Available: <https://www.nature.com/articles/44348.pdf>.
- [3] C. H. van der Wal, A. C. J. ter Haar, F. K. Wilhelm, R. N. Schouten, C. J. P. M. Harman, T. P. Orlando, S. Lloyd, and J. E. Mooij, “Quantum Superposition of Macroscopic Persistent-Current States,” *Science*, vol. 290, no. 5492, pp. 773–777, 2000, ISSN: 00368075, 10959203. [Online]. Available: <http://www.jstor.org/stable/3078179> (visited on 07/22/2022).
- [4] H. Pino, J. Prat-Camps, K. Sinha, B. P. Venkatesh, and O. Romero-Isart, “On-chip quantum interference of a superconducting microsphere,” 2016. DOI: [10.48550/ARXIV.1603.01553](https://doi.org/10.48550/ARXIV.1603.01553). [Online]. Available: <https://arxiv.org/abs/1603.01553>.
- [5] U. Delić, M. Reisenbauer, K. Dare, D. Grass, V. Vuletić, N. Kiesel, and M. Aspelmeyer, “Cooling of a levitated nanoparticle to the motional quantum ground state,” *Science*, vol. 367, no. 6480, pp. 892–895, 2020. DOI: [10.1126/science.aba3993](https://doi.org/10.1126/science.aba3993). eprint: <https://www.science.org/doi/pdf/10.1126/science.aba3993>. [Online]. Available: <https://www.science.org/doi/abs/10.1126/science.aba3993>.
- [6] Y. Y. Fein, P. Geyer, P. Zwick, F. Kiałka, S. Pedalino, M. Mayor, S. Gerlich, and M. Arndt, “Quantum superposition of molecules beyond 25 kda,” *Nature Physics*, vol. 15, no. 12, pp. 1242–1245, Sep. 2019. DOI: [10.1038/s41567-019-0663-9](https://doi.org/10.1038/s41567-019-0663-9). [Online]. Available: <https://www.nature.com/articles/s41567-019-0663-9.pdf>.
- [7] F. Monteiro, S. Ghosh, A. G. Fine, and D. C. Moore, “Optical levitation of 10-ng spheres with nano- $g$  acceleration sensitivity,” *Physical Review A*, vol. 96, no. 6, Oct. 2017. DOI: [10.1103/physreva.96.063841](https://doi.org/10.1103/physreva.96.063841). [Online]. Available: <https://journals.aps.org/prapdf/10.1103/PhysRevA.96.063841>.
- [8] O. Romero-Isart, L. Clemente, C. Navau, A. Sanchez, and J. I. Cirac, “Quantum magnetomechanics with levitating superconducting microspheres,” *Physical Review Letters*, vol. 109, no. 14, Oct. 2012. DOI: [10.1103/physrevlett.109.147205](https://doi.org/10.1103/physrevlett.109.147205). [Online]. Available: <https://journals.aps.org/prl/pdf/10.1103/PhysRevLett.109.147205>.
- [9] C. Kittel, *Introduction to solid state physics*, 8th ed. Hoboken, NJ: Wiley, 2005, ch. 10 Superconductivity.
- [10] M. Tinkham, *Introduction to Superconductivity: Second Edition*, ser. Dover Books on Physics. Dover Publications, 2004, ISBN: 9780486435039.
- [11] T. Van Duzer and C. W. Turner, “Principles of superconductive devices and circuits,” in, 2nd ed. Philadelphia, PA: Prentice Hall, 1998, ch. 5 Electronics Application.
- [12] M. Göppl, A. Fregner, M. Baur, R. Bianchetti, S. Filipp, J. M. Fink, P. J. Leek, G. Puebla, L. Steffen, and A. Wallraff, “Coplanar waveguide resonators for circuit quantum electrodynamics,” *Journal of Applied Physics*, vol. 104, no. 11, p. 113 904, Dec. 2008. DOI: [10.1063/1.3010859](https://doi.org/10.1063/1.3010859). [Online]. Available: <https://doi.org/10.1063/1.3010859>.
- [13] K. Seeger, “Microwave dielectric constants of silicon, gallium arsenide, and quartz,” *Journal of Applied Physics*, vol. 63, no. 11, pp. 5439–5443, 1988. DOI: [10.1063/1.341153](https://doi.org/10.1063/1.341153). eprint: <https://doi.org/10.1063/1.341153>. [Online]. Available: <https://doi.org/10.1063/1.341153>.

- [14] K. Watanabe, K. Yoshida, T. Aoki, and S. Kohjiro, “Kinetic inductance of superconducting coplanar waveguides,” *Japanese Journal of Applied Physics*, vol. 33, no. Part 1, No. 10, pp. 5708–5712, Oct. 1994. DOI: [10.1143/jjap.33.5708](https://doi.org/10.1143/jjap.33.5708). [Online]. Available: <https://iopscience.iop.org/article/10.1088/1742-6596/97/1/012044/pdf>.
- [15] S. Gevorgian, T. Martinsson, P. Linner, and E. Kollberg, “Cad models for multilayered substrate interdigital capacitors,” *IEEE Transactions on Microwave Theory and Techniques*, vol. 44, no. 6, pp. 896–904, 1996. DOI: [10.1109/22.506449](https://doi.org/10.1109/22.506449).
- [16] D. M. Pozar, *Microwave Engineering*, English, Hardcover. Wiley, Nov. 2011, ISBN: 978-0470631553.
- [17] M. Golio and J. Golio, Eds., *RF and Microwave Passive and Active Technologies (The RF and Microwave Handbook, Second Edition)*. CRC Press, Dec. 2007, ISBN: 978-0849372209.
- [18] S. Doyle, P. Mauskopf, J. Naylor, A. Porch, and C. Duncombe, “Lumped element kinetic inductance detectors,” *Journal of Low Temperature Physics*, vol. 151, no. 1-2, pp. 530–536, Jan. 2008. DOI: [10.1007/s10909-007-9685-2](https://doi.org/10.1007/s10909-007-9685-2). [Online]. Available: <https://doi.org/10.1007/s10909-007-9685-2>.
- [19] R. Barends, *Photon-detecting superconducting resonators*. Delft: Barends, 2009, ISBN: 978-90-8593-052-5.
- [20] M. S. Khalil, M. J. A. Stoutimore, F. C. Wellstood, and K. D. Osborn, “An analysis method for asymmetric resonator transmission applied to superconducting devices,” *Journal of Applied Physics*, vol. 111, no. 5, p. 054510, Mar. 2012. DOI: [10.1063/1.3692073](https://doi.org/10.1063/1.3692073). [Online]. Available: <https://doi.org/10.1063/1.3692073>.
- [21] S. Probst, F. B. Song, P. A. Bushev, A. V. Ustinov, and M. Weides, “Efficient and robust analysis of complex scattering data under noise in microwave resonators,” *Review of Scientific Instruments*, vol. 86, no. 2, p. 024706, Feb. 2015. DOI: [10.1063/1.4907935](https://doi.org/10.1063/1.4907935). [Online]. Available: <https://doi.org/10.1063/1.4907935>.
- [22] M. Wallquist, V. S. Shumeiko, and G. Wendin, “Selective coupling of superconducting charge qubits mediated by a tunable stripline cavity,” *Physical Review B*, vol. 74, no. 22, Dec. 2006. DOI: [10.1103/physrevb.74.224506](https://doi.org/10.1103/physrevb.74.224506). [Online]. Available: <https://doi.org/10.1103/physrevb.74.224506>.
- [23] S. Pogorzalek, K. G. Fedorov, L. Zhong, J. Goetz, F. Wulschner, M. Fischer, P. Eder, E. Xie, K. Inomata, T. Yamamoto, Y. Nakamura, A. Marx, F. Deppe, and R. Gross, “Hysteretic flux response and nondegenerate gain of flux-driven josephson parametric amplifiers,” *Physical Review Applied*, vol. 8, no. 2, Aug. 2017. DOI: [10.1103/physrevapplied.8.024012](https://doi.org/10.1103/physrevapplied.8.024012). [Online]. Available: <https://doi.org/10.1103/physrevapplied.8.024012>.
- [24] M. Gutierrez, A. Paradkar, D. Hambreus, G. Higgins, and W. Wieczorek, “A chip-based superconducting magnetic trap for levitating superconducting microparticles,” *IEEE Transactions on Applied Superconductivity*, vol. 32, no. 4, pp. 1–5, Jun. 2022. DOI: [10.1109/tasc.2022.3147730](https://doi.org/10.1109/tasc.2022.3147730). [Online]. Available: <https://doi.org/10.1109/tasc.2022.3147730>.
- [25] A. Vinante, P. Falferi, G. Gasbarri, A. Setter, C. Timberlake, and H. Ulbricht, “Ultralow mechanical damping with meissner-levitated ferromagnetic microparticles,” *Phys. Rev. Applied*, vol. 13, p. 064027, 6 Jun. 2020. DOI: [10.1103/PhysRevApplied.13.064027](https://doi.org/10.1103/PhysRevApplied.13.064027). [Online]. Available: <https://link.aps.org/doi/10.1103/PhysRevApplied.13.064027>.
- [26] J. Gieseler, A. Kabcenell, E. Rosenfeld, J. D. Schaefer, A. Safira, M. J. A. Schuetz, C. Gonzalez-Ballester, C. C. Rusconi, O. Romero-Isart, and M. D. Lukin, “Single-spin magnetomechanics with levitated micromagnets,” *Phys. Rev. Lett.*, vol. 124, p. 163604, 16 Apr. 2020. DOI: [10.1103/PhysRevLett.124.163604](https://doi.org/10.1103/PhysRevLett.124.163604). [Online]. Available: <https://link.aps.org/doi/10.1103/PhysRevLett.124.163604>.
- [27] M. D. Simon and A. K. Geim, “Diamagnetic levitation: Flying frogs and floating magnets (invited),” *Journal of Applied Physics*, vol. 87, no. 9, pp. 6200–6204, May 2000. DOI: [10.1063/1.372654](https://doi.org/10.1063/1.372654). [Online]. Available: <https://doi.org/10.1063/1.372654>.
- [28] L. Magrini, P. Rosenzweig, C. Bach, A. Deutschmann-Olek, S. G. Hofer, S. Hong, N. Kiesel, A. Kugi, and M. Aspelmeyer, “Real-time optimal quantum control of mechanical motion at room temperature,” *Nature*, vol. 595, no. 7867, pp. 373–377, Jul. 2021. DOI: [10.1038/s41586-021-03602-3](https://doi.org/10.1038/s41586-021-03602-3). [Online]. Available: <https://doi.org/10.1038/s41586-021-03602-3>.
- [29] D. Zoepfl, M. Juan, C. Schneider, and G. Kirchmair, “Single-photon cooling in microwave magnetomechanics,” *Physical Review Letters*, vol. 125, no. 2, Jul. 2020. DOI: [10.1103/](https://doi.org/10.1103/)

- physrevlett.125.023601. [Online]. Available: <https://doi.org/10.1103/physrevlett.125.023601>.
- [30] I. C. Rodrigues, D. Bothner, and G. A. Steele, “Coupling microwave photons to a mechanical resonator using quantum interference,” *Nature Communications*, vol. 10, no. 1, p. 5359, Nov. 2019, ISSN: 2041-1723. DOI: [10.1038/s41467-019-12964-2](https://doi.org/10.1038/s41467-019-12964-2). [Online]. Available: <https://doi.org/10.1038/s41467-019-12964-2>.
- [31] G. Ventura and L. Risegari, *The art of cryogenics: low-temperature experimental techniques*, en, 1st ed. Amsterdam ; Boston: Elsevier, 2008, p. 133, OCLC: ocn190861238, ISBN: 978-0-08-044479-6.
- [32] A. Osman, J. Simon, A. Bengtsson, S. Kosen, P. Krantz, D. P. Lozano, M. Scigliuzzo, P. Delsing, J. Bylander, and A. F. Roudsari, “Simplified josephson-junction fabrication process for reproducibly high-performance superconducting qubits,” *Applied Physics Letters*, vol. 118, no. 6, p. 064002, Feb. 2021. DOI: [10.1063/5.0037093](https://doi.org/10.1063/5.0037093). [Online]. Available: <https://doi.org/10.1063/5.0037093>.
- [33] A. Ramzi, S. A. Charlebois, and P. Krantz, “Niobium and aluminum josephson junctions fabricated with a damascene cmp process,” *Physics Procedia*, vol. 36, pp. 211–216, 2012, SUPERCONDUCTIVITY CENTENNIAL Conference 2011, ISSN: 1875-3892. DOI: <https://doi.org/10.1016/j.phpro.2012.06.148>. [Online]. Available: <https://www.sciencedirect.com/science/article/pii/S1875389212020858>.
- [34] J. Romijn, T. M. Klapwijk, M. J. Renne, and J. E. Mooij, “Critical pair-breaking current in superconducting aluminum strips far below  $T_c$ ,” *Phys. Rev. B*, vol. 26, pp. 3648–3655, 7 Oct. 1982. DOI: [10.1103/PhysRevB.26.3648](https://doi.org/10.1103/PhysRevB.26.3648). [Online]. Available: <https://link.aps.org/doi/10.1103/PhysRevB.26.3648>.
- [35] D. Shen, R. Zhu, W. Xu, J. Chang, Z. Ji, G. Sun, C. Cao, and J. Chen, “Character and fabrication of Al/Al<sub>2</sub>O<sub>3</sub>/Al tunnel junctions for qubit application,” *Chinese Science Bulletin*, vol. 57, no. 4, pp. 409–412, Feb. 2012, ISSN: 1861-9541. DOI: [10.1007/s11434-011-4821-4](https://doi.org/10.1007/s11434-011-4821-4). [Online]. Available: <https://doi.org/10.1007/s11434-011-4821-4>.
- [36] D. Niepce, *Superinductance and fluctuating two-level systems: loss and noise in disordered and non-disordered superconducting quantum devices*, eng, ser. Doktorsavhandlingar vid Chalmers tekniska högskola Ny serie nr 4779. Gothenburg, Sweden: Chalmers University of Technology, 2020, ISBN: 978-91-7905-312-3.
- [37] M. Von Schickfus and S. Hunklinger, “Saturation of the dielectric absorption of vitreous silica at low temperatures,” *Physics Letters A*, vol. 64, no. 1, pp. 144–146, 1977, ISSN: 0375-9601. DOI: [https://doi.org/10.1016/0375-9601\(77\)90558-8](https://doi.org/10.1016/0375-9601(77)90558-8). [Online]. Available: <https://www.sciencedirect.com/science/article/pii/0375960177905588>.
- [38] Q. He, P. OuYang, H. Gao, S. He, Y. Li, Y. Wang, Y. Chen, X. Dai, Y. Wang, and L. F. Wei, “Low-loss superconducting aluminum microwave coplanar waveguide resonators on sapphires for the qubit readouts,” *Superconductor Science and Technology*, vol. 35, no. 6, p. 065017, May 2022. DOI: [10.1088/1361-6668/ac6a1d](https://doi.org/10.1088/1361-6668/ac6a1d). [Online]. Available: <https://doi.org/10.1088/1361-6668/ac6a1d>.
- [39] D. Kalacheva, G. Fedorov, A. Kulakova, J. Zotova, E. Korostylev, I. Khrapach, A. V. Ustinov, and O. V. Astafiev, “Improving the quality factor of superconducting resonators by post-process surface treatment,” *AIP Conference Proceedings*, vol. 2241, no. 1, p. 020018, 2020. DOI: [10.1063/5.0011900](https://doi.org/10.1063/5.0011900). eprint: <https://aip.scitation.org/doi/pdf/10.1063/5.0011900>. [Online]. Available: <https://aip.scitation.org/doi/abs/10.1063/5.0011900>.
- [40] J. M. Sage, V. Bolkhovsky, W. D. Oliver, B. Turek, and P. B. Welander, “Study of loss in superconducting coplanar waveguide resonators,” *Journal of Applied Physics*, vol. 109, no. 6, p. 063915, Mar. 2011. DOI: [10.1063/1.3552890](https://doi.org/10.1063/1.3552890). [Online]. Available: <https://doi.org/10.1063/1.3552890>.
- [41] A. Megrant, C. Neill, R. Barends, B. Chiaro, Y. Chen, L. Feigl, J. Kelly, E. Lucero, M. Mariantoni, P. J. J. O’Malley, D. Sank, A. Vainsencher, J. Wenner, T. C. White, Y. Yin, J. Zhao, C. J. Palmstrøm, J. M. Martinis, and A. N. Cleland, “Planar superconducting resonators with internal quality factors above one million,” *Applied Physics Letters*, vol. 100, no. 11, p. 113510, 2012. DOI: [10.1063/1.3693409](https://doi.org/10.1063/1.3693409). eprint: <https://doi.org/10.1063/1.3693409>. [Online]. Available: <https://doi.org/10.1063/1.3693409>.
- [42] M. D. Maloney, F. de la Cruz, and M. Cardona, “Superconducting parameters and size effects of aluminum films and foils,” *Phys. Rev. B*, vol. 5, pp. 3558–3572, 9 May 1972. DOI:

- 10.1103/PhysRevB.5.3558. [Online]. Available: <https://link.aps.org/doi/10.1103/PhysRevB.5.3558>.
- [43] Y. Asada and H. Nosé, “Superconductivity of niobium films,” *Journal of the Physical Society of Japan*, vol. 26, no. 2, pp. 347–354, 1969. DOI: [10.1143/JPSJ.26.347](https://doi.org/10.1143/JPSJ.26.347). eprint: <https://doi.org/10.1143/JPSJ.26.347>. [Online]. Available: <https://doi.org/10.1143/JPSJ.26.347>.

# A

## Appendix A

### A.1 Full derivation from $Z_{TLR}$ to $S_{21}(\omega_0)$

In this appendix chapter, the full derivation to Equation (2.59) is presented, starting from Equation (2.32)

$$\begin{aligned}
 Z_{TLR} &= Z_0 \tanh(\gamma l) = \\
 &= Z_0 \tanh((\alpha + i\beta)l) = Z_0 \frac{\tanh(\alpha l) + \tanh(i\beta l)}{1 + \tanh(\alpha l) \tanh(i\beta l)} = \\
 &= Z_0 \frac{\tanh(\alpha l) + i \tanh(\beta l)}{1 + \tanh(\alpha l) i \tanh(\beta l)} = Z_0 \frac{\tanh(\alpha l) - \frac{1}{i \cot(\beta l)}}{1 - \frac{\tanh(\alpha l)}{i \cot(\beta l)}} = \\
 &= Z_0 \frac{1 - i \tanh(\alpha l) \cot(\beta l)}{\tanh(\alpha l) - i \cot(\beta l)}. \tag{A.1}
 \end{aligned}$$

The fundamental wavelength is  $l = \lambda_0/4$  such that  $\beta l$  at near resonance will be

$$\begin{aligned}
 \beta l &= \frac{\omega + \delta\omega}{\nu} \frac{\lambda_0}{4} = \frac{2\pi(\omega + \delta\omega)}{\lambda_0 \omega} \frac{\lambda_0}{4} \\
 &= \frac{\pi(\omega + \delta\omega)}{2\omega} = \frac{\pi}{2} \left( 1 + \frac{\delta\omega}{\omega} \right), \tag{A.2}
 \end{aligned}$$

where  $\delta\omega$  is the detuned frequency near resonance. Plugging in above expression for  $\beta l$  in  $\cot(\beta l)$  gives

$$\cot(\beta l) = \frac{\cos(\beta l)}{\sin(\beta l)} = \frac{\cos\left(\frac{\pi}{2} \left(1 + \frac{\delta\omega}{\omega}\right)\right)}{\sin\left(\frac{\pi}{2} \left(1 + \frac{\delta\omega}{\omega}\right)\right)} = -\frac{\sin\left(\frac{\pi}{2} \frac{\delta\omega}{\omega}\right)}{\cos\left(\frac{\pi}{2} \frac{\delta\omega}{\omega}\right)} = \tan\left(-\frac{\pi}{2} \frac{\delta\omega}{\omega}\right) \approx -\frac{\pi}{2} \frac{\delta\omega}{\omega} \tag{A.3}$$

in which the small-angle approximation was utilized in the last step of the evaluation. From Equation (2.31) it is known that  $Q_i = \frac{\beta}{2\alpha}$ , such that  $\tanh(\alpha l)$  under the small-angle approximation gives

$$\tanh(\alpha l) = \tanh\left(\frac{\beta}{2Q_i} l\right) = \tanh\left(\frac{1}{2Q_i} \frac{\pi}{2} \left(1 + \frac{\delta\omega}{\omega}\right)\right) \approx \frac{1}{2Q_i} \frac{\pi}{2} \left(1 + \frac{\delta\omega}{\omega}\right) \tag{A.4}$$

Considering an unloaded resonator for which the resonance frequency is  $\omega_{1/4}$ , such that  $\delta\omega = \delta\omega_{1/4}$ , Equation (A.1) will then express at near resonance as

$$Z_{TLR} = Z_0 \frac{1 - i \tanh(\alpha l) \cot(\beta l)}{\tanh(\alpha l) - i \cot(\beta l)} = Z_0 \frac{1 - i \left(\frac{1}{2Q_i} \frac{\pi}{2} \left(1 + \frac{\delta\omega_{1/4}}{\omega_{1/4}}\right)\right) \left(-\frac{\pi}{2} \frac{\delta\omega_{1/4}}{\omega_{1/4}}\right)}{\frac{1}{2Q_i} \frac{\pi}{2} \left(1 + \frac{\delta\omega_{1/4}}{\omega_{1/4}}\right) - i \left(-\frac{\pi}{2} \frac{\delta\omega_{1/4}}{\omega_{1/4}}\right)}, \tag{A.5}$$

for which,  $\left(1 + \frac{\delta\omega_{1/4}}{\omega_{1/4}}\right) \approx 1$  since  $\frac{\delta\omega_{1/4}}{\omega_{1/4}} \ll 1$ . With this approximation, it is found that

$$\begin{aligned}
Z_{TLR} &= Z_0 \frac{1 + i \left( \frac{1}{2Q_i} \frac{\pi^2}{4} \frac{\delta\omega_{1/4}}{\omega_{1/4}} \right)}{\frac{1}{2Q_i} \frac{\pi}{2} \left( 1 + i2Q_i \frac{\delta\omega_{1/4}}{\omega_{1/4}} \right)} = Z_0 \frac{\frac{4Q_i}{\pi} + i \frac{\pi}{2} \frac{\delta\omega_{1/4}}{\omega_{1/4}}}{1 + i2Q_i \frac{\delta\omega_{1/4}}{\omega_{1/4}}} \\
&\approx Z_0 \frac{\frac{4Q_i}{\pi}}{1 + i2Q_i \frac{\delta\omega_{1/4}}{\omega_{1/4}}} = Z_0 \frac{\frac{4Q_i}{\pi} - i \frac{8Q_i^2}{\pi} \frac{\delta\omega_{1/4}}{\omega_{1/4}}}{1 + 4Q_i^2 \left( \frac{\delta\omega_{1/4}}{\omega_{1/4}} \right)^2}, \tag{A.6}
\end{aligned}$$

which is the same as Equation (2.34). The total impedance is expressed in Equation (2.35). By plugging in  $Q_C$  from (2.40) into (2.35) the following is derived

$$\frac{Z}{Z_0} = \frac{\frac{4Q_i}{\pi} - i \frac{8Q_i^2}{\pi} \frac{\delta\omega_{1/4}}{\omega_{1/4}}}{1 + 4Q_i^2 \left( \frac{\delta\omega_{1/4}}{\omega_{1/4}} \right)^2} - i \frac{1}{Z_0 \omega C_C} = \frac{\frac{4Q_i}{\pi} - i \frac{8Q_i^2}{\pi} \frac{\delta\omega_{1/4}}{\omega_{1/4}}}{1 + 4Q_i^2 \left( \frac{\delta\omega_{1/4}}{\omega_{1/4}} \right)^2} - i \sqrt{\frac{2Q_C}{\pi}} \tag{A.7}$$

$$= \frac{\frac{4Q_i}{\pi} - i \frac{8Q_i^2}{\pi} \frac{\delta\omega_{1/4}}{\omega_{1/4}} - i \sqrt{\frac{2Q_C}{\pi}} \left[ 1 + 4Q_i^2 \left( \frac{\delta\omega_{1/4}}{\omega_{1/4}} \right)^2 \right]}{1 + 4Q_i^2 \left( \frac{\delta\omega_{1/4}}{\omega_{1/4}} \right)^2}, \tag{A.8}$$

which is the same as Equation (2.41). It is known that at resonance,  $\text{Im}(Z) = 0$ , meaning

$$4Q_i^2 \sqrt{\frac{2Q_C}{\pi}} \left( \frac{\delta\omega_{1/4}}{\omega_{1/4}} \right)^2 + \frac{8Q_i^2}{\pi} \left( \frac{\delta\omega_{1/4}}{\omega_{1/4}} \right) + \sqrt{\frac{2Q_C}{\pi}} = 0,$$

whereby solving for  $\delta\omega_{1/4}/\omega_{1/4}$  gives

$$\begin{aligned}
\frac{\delta\omega_{1/4}}{\omega_{1/4}} &= -\frac{1}{\pi} \sqrt{\frac{\pi}{2Q_C}} \pm \sqrt{\frac{1}{\pi^2} \frac{\pi}{2Q_C} - \frac{1}{4Q_i^2}} \approx -\frac{1}{\pi} \sqrt{\frac{\pi}{2Q_C}} \pm \sqrt{\frac{1}{\pi^2} \frac{\pi}{2Q_C}} \\
&\implies \frac{\delta\omega_{1/4}}{\omega_{1/4}} = -\sqrt{\frac{2}{\pi Q_C}}
\end{aligned}$$

under the assumption that  $1/4Q_i^2$  is negligibly small.

To reach Equation (2.43), the denominator of (A.7) is factorized such that

$$\begin{aligned}
\frac{Z}{Z_0} &= \frac{\frac{4Q_i}{\pi} - i \frac{8Q_i^2}{\pi} \frac{\delta\omega_{1/4}}{\omega_{1/4}}}{1 + 4Q_i^2 \left( \frac{\delta\omega_{1/4}}{\omega_{1/4}} \right)^2} - i \sqrt{\frac{2Q_C}{\pi}} \\
&= \frac{\frac{4Q_i}{\pi} \left[ 1 - i2Q_i \left( \frac{\delta\omega_{1/4}}{\omega_{1/4}} \right) \right]}{\left[ 1 + i2Q_i \left( \frac{\delta\omega_{1/4}}{\omega_{1/4}} \right) \right] \left[ 1 - i2Q_i \left( \frac{\delta\omega_{1/4}}{\omega_{1/4}} \right) \right]} - i \sqrt{\frac{2Q_C}{\pi}} \\
&= \frac{\frac{4Q_i}{\pi}}{1 + i2Q_i \left( \frac{\delta\omega_{1/4}}{\omega_{1/4}} \right)} - i \sqrt{\frac{2Q_C}{\pi}} = \frac{\frac{4Q_i}{\pi} - i \sqrt{\frac{2Q_C}{\pi}} \left( 1 + i2Q_i \left( \frac{\delta\omega_{1/4}}{\omega_{1/4}} \right) \right)}{1 + i2Q_i \left( \frac{\delta\omega_{1/4}}{\omega_{1/4}} \right)^2} \\
&= \sqrt{\frac{2Q_C}{\pi}} \frac{\frac{4Q_i}{\pi} \sqrt{\frac{\pi}{2Q_C}} - i \left( 1 + i2Q_i \left( \frac{\delta\omega_{1/4}}{\omega_{1/4}} \right) \right)}{1 + i2Q_i \left( \frac{\delta\omega_{1/4}}{\omega_{1/4}} \right)} \\
&= \sqrt{\frac{2Q_C}{\pi}} \frac{\frac{4Q_i}{\pi} \sqrt{\frac{\pi}{2Q_C}} - i \left( 1 + i2Q_i \left( \frac{\delta\omega_0}{\omega_0} - \sqrt{\frac{2}{\pi Q_C}} \right) \right)}{1 + i2Q_i \left( \frac{\delta\omega_0}{\omega_0} \right) - i2Q_i \sqrt{\frac{2}{\pi Q_C}}} \\
&= \sqrt{\frac{2Q_C}{\pi}} \frac{2Q_i \left( \frac{\delta\omega_0}{\omega_0} \right) - i}{1 + i2Q_i \left( \frac{\delta\omega_0}{\omega_0} \right) - i2Q_i \sqrt{\frac{2}{\pi Q_C}}}, \tag{A.9}
\end{aligned}$$

which is the same as (2.43). Thus, an expression is found for  $Z/Z_0$  in terms of  $\omega_0$  at near resonance.

$S_{21}(\omega_0)$  is found by simplifying (A.9) through multiplying the expression with the complex conjugate:

$$\begin{aligned} Z &= Z_0 \sqrt{\frac{2Q_C}{\pi}} \frac{2Q_i \left( \frac{\delta\omega_0}{\omega_0} \right) - i}{1 + i \left( 2Q_i \left( \frac{\delta\omega_0}{\omega_0} \right) - 2Q_i \sqrt{\frac{2}{\pi Q_C}} \right)} \cdot \frac{1 - i \left( 2Q_i \left( \frac{\delta\omega_0}{\omega_0} \right) - 2Q_i \sqrt{\frac{2}{\pi Q_C}} \right)}{1 - i \left( 2Q_i \left( \frac{\delta\omega_0}{\omega_0} \right) - 2Q_i \sqrt{\frac{2}{\pi Q_C}} \right)} \\ &= Z_0 \sqrt{\frac{2Q_C}{\pi}} \frac{2Q_i \left( \frac{\delta\omega_0}{\omega_0} \right) - i 2Q_i \left( \frac{\delta\omega_0}{\omega_0} \right) \left( 2Q_i \left( \frac{\delta\omega_0}{\omega_0} \right) - 2Q_i \sqrt{\frac{2}{\pi Q_C}} \right) - i - \left( 2Q_i \left( \frac{\delta\omega_0}{\omega_0} \right) - 2Q_i \sqrt{\frac{2}{\pi Q_C}} \right)}{1 + \left( 2Q_i \left( \frac{\delta\omega_0}{\omega_0} \right) - 2Q_i \sqrt{\frac{2}{\pi Q_C}} \right)^2}. \end{aligned}$$

Assuming resonance, the above expression can be simplified to

$$Z = Z_0 \sqrt{\frac{2Q_C}{\pi}} \frac{2Q_i \sqrt{\frac{2}{\pi Q_C}}}{1 + \left( -2Q_i \sqrt{\frac{2}{\pi Q_C}} \right)^2} \approx Z_0 \sqrt{\frac{2Q_C}{\pi}} \frac{2Q_i \sqrt{\frac{2}{\pi Q_C}}}{4Q_i^2 \frac{2}{\pi Q_C}},$$

under the approximation  $1 \ll 4Q_i^2 \frac{2}{\pi Q_C}$ . Plugging in the above expression into the definition of  $S_{21}$  yields the following

$$\begin{aligned} S_{21}(\omega_0) &= \frac{2}{2 + Z_0/Z} = \frac{2}{2 + \frac{1}{\frac{\sqrt{\frac{2Q_C}{\pi}} \frac{2Q_i \sqrt{\frac{2}{\pi Q_C}}}{4Q_i^2 \frac{2}{\pi Q_C}}}}}} \\ &= \frac{2}{2 + \frac{4Q_i^2 \frac{2}{\pi}}{2Q_i}} = \frac{1}{1 + \frac{Q_i}{Q_C}} = \frac{Q_C}{Q_C + Q_i}, \end{aligned}$$

which is Equation (2.47).



# B

## Appendix B

### B.1 Current density and CPW resonator fabrication

#### B.1.1 Aluminum

- a) Wafer cleaning
  - (i) Take 2" Si wafer with  $\langle 111 \rangle$  orientation & high resistivity ( $\rho = 10 \text{ k}\Omega \cdot \text{cm}$ )
  - (ii) Clean with acetone & IPA
  - (iii) Blow dry with  $\text{N}_2$
  - (iv) Dip in 2% HF solution for 1 min
  - (v) Quick Dump Rinse in fresh DI water
- b) Ground plane deposition
  - (i) Sputter Al in FHR-MS150
    - Thickness: 150 nm
    - Pressure: 8  $\mu\text{bar}$
    - Deposition rate: 2 nm/s
    - Deposition time: 75 s
- c) Ground plane patterning
  - (i) Spin coat S1805 [600 nm]
    - Time: 60 seconds
    - Speed: 4000 rpm
    - Acceleration: 2000
  - (ii) Resist baking
    - Time: 2 minutes
    - Temperature: 120  $^\circ\text{C}$
  - (iii) Expose on DWL Laser Writer (Heidelberg 2000)
    - Focus: 40%
    - Intensity: 70%
    - Transmission: 100%
  - (iv) Develop in MF319 for 90 seconds
  - (v) Descumming with Oxygen Plasma
    - Time: 10 minutes
    - Power: 40 W
  - (vi) Aluminum Etch for 120 sec at 40  $^\circ\text{C}$
  - (vii) Clean with Remover 1165 followed by Acetone & IPA on hotplate at 80  $^\circ\text{C}$  for 5 minutes & Ultrasound for 5 minutes

#### B.1.2 Niobium

- a) Wafer cleaning
  - (i) Take 2" Si wafer with  $\langle 111 \rangle$  orientation & high resistivity ( $\rho = 10 \text{ k}\Omega \cdot \text{cm}$ )
  - (ii) Clean with acetone & IPA
  - (iii) Blow dry with  $\text{N}_2$
  - (iv) Dip in 2% HF solution for 1 min
  - (v) Quick Dump Rinse in fresh DI water
- b) Ground plane deposition
  - (i) Sputter Nb in FHR-MS150
    - Thickness: 150 nm

- Pressure: 0.3  $\mu$ bar
- Deposition rate: 8 nm/s
- Deposition time: 20 s
- c) Ground plane patterning
  - (i) Spin coat S1805 [600 nm]
    - Time: 60 seconds
    - Speed: 4000 rpm
    - Acceleration: 2000
  - (ii) Resist baking
    - Time: 2 minutes
    - Temperature: 120 °C
  - (iii) Expose on DWL Laser Writer (Heidelberg 2000)
    - Focus: 40%
    - Intensity: 70%
    - Transmission: 100%
  - (iv) Develop in MF319 for 90 seconds
  - (v) Descumming with Oxygen Plasma
    - Time: 10 minutes
    - Power: 40 W
  - (vi) Aluminum Etch for 120 sec at 40 °C
  - (vii) Clean with Remover 1165 followed by Acetone & IPA on hotplate at 80 °C for 5 minutes & Ultrasound for 5 minutes



**CHALMERS**  
UNIVERSITY OF TECHNOLOGY